HHS Public Access

Author manuscript

Cell Metab. Author manuscript; available in PMC 2021 February 04.

Published in final edited form as:

Cell Metab. 2020 February 04; 31(2): 284–300.e7. doi:10.1016/j.cmet.2019.11.002.

Regulation of Tumor Initiation by the Mitochondrial Pyruvate Carrier

Claire L. Bensard[1,†], **Dona R. Wisidagama**[2,†], **Kristofor A. Olson**[1,††], **Jordan A. Berg**[1], **Nathan M. Krah**[2], **John C. Schell**[1,†††], **Sara M. Nowinski**[1], **Sarah Fogarty**[1], **Alex J. Bott**[1], **Peng Wei**[1], **Katja K. Dove**[1], **Jason M. Tanner**[1], **Vanja Panic**[1], **Ahmad Cluntun**[1], **Sandra Lettlova**[1], **Christian S. Earl**[1], **David F. Namnath**[1], **Karina Vázquez-Arregun**[3], **Claudio J. Villanueva**[1], **Dean Tantin**[3], **L. Charles Murtaugh**[2], **Kimberley J. Evason**[3,4], **Gregory S. Ducker**[1], **Carl S. Thummel**[2,*], **Jared Rutter**[1,5,*]

[1]Department of Biochemistry, University of Utah SLC, UT 84132, USA

[2]Department of Human Genetics, University of Utah, SLC, UT 84132, USA

[3]Department of Pathology, University of Utah, SLC, UT 84132, USA

[4]Huntsman Cancer Institute, University of Utah, SLC, UT 84132, USA

[5]Howard Hughes Medical Institute, University of Utah School of Medicine, SLC, UT 84132, USA

Summary

While metabolic adaptations have been demonstrated to be essential for tumor cell proliferation, the metabolic underpinnings of tumor initiation are poorly understood. We found that the earliest stages of colorectal cancer (CRC) initiation are marked by a glycolytic metabolic signature, including down-regulation of the mitochondrial pyruvate carrier (MPC), which couples glycolysis and glucose oxidation through mitochondrial pyruvate import. Genetic studies in *Drosophila*

*Correspondence rutter@biochem.utah.edu (JR)—Lead contact; carl.thummel@genetics.utah.edu (CST).

††Current Address: Department of Surgery and Perioperative Care, Dell Medical School, University of Texas, Austin, TX 78712, USA

†††Current Address: Department of Medicine, Massachusetts General Hospital, Boston MA, 02114

Author contributions

CLB and KAO designed the mouse experimental strategy with input from JCS, PW, AC, KD, JMT, CJV, DT, LCM, KJE and JR. DRW designed and performed the fly experiments with input and supervision from CST. CLB and KAO, with help from CSE and DFN, performed MPC1 mouse homeostatic experiments and data analysis. CLB, with help from CSE and DFN, performed all tumor initiation experiments and data analysis from mouse studies. CLB, KAO, NMK, KJE, and LCM performed histological staining and imaging of mouse tissue. CLB, SF, and VP quantified tumor proliferation indices. KJE and CLB assessed all histology. SMN performed protein validation by immunoblots. KVA and DT contributed supplemental samples. CLB, CSE, DFN, and KAO maintained mouse colony. CLB, JAB, and AJB designed human gene expression experiment. CLB with input from GSD, AC, and JR designed the metabolomics experiments and collected all data with assistance from SF, PW, KD, AC, SL, and AJB. GSD performed all metabolomic experiments and data analysis. JAB and AJB designed and performed all bioinformatics analyses. CLB and DRW, with contributions from SF, KAO, JAB and AJB, made all figures. CLB, DRW, CST and JR wrote the manuscript with input from NMK, KJE, SF, DT, and SMN. All work was performed at the University of Utah.

†These authors contributed equally to this work

Declaration of Interests

The University of Utah has filed a patent related to the Mitochondrial Pyruvate Carrier, of which JR and CST are listed as co-inventors. All other authors have no competing interests to declare.

suggest that this downregulation is required since hyperplasia caused by loss of the *Apc* or *Notch* tumor suppressors in intestinal stem cells can be completely blocked by *MPC* overexpression. Moreover, in two distinct CRC mouse models, loss of *Mpc1* prior to a tumorigenic stimulus doubled the frequency of adenoma formation and produced higher grade tumors. MPC loss was associated with a glycolytic metabolic phenotype and increased expression of stem cell markers. These data suggest that changes in cellular pyruvate metabolism are necessary and sufficient to promote cancer initiation.

Graphical Abstract

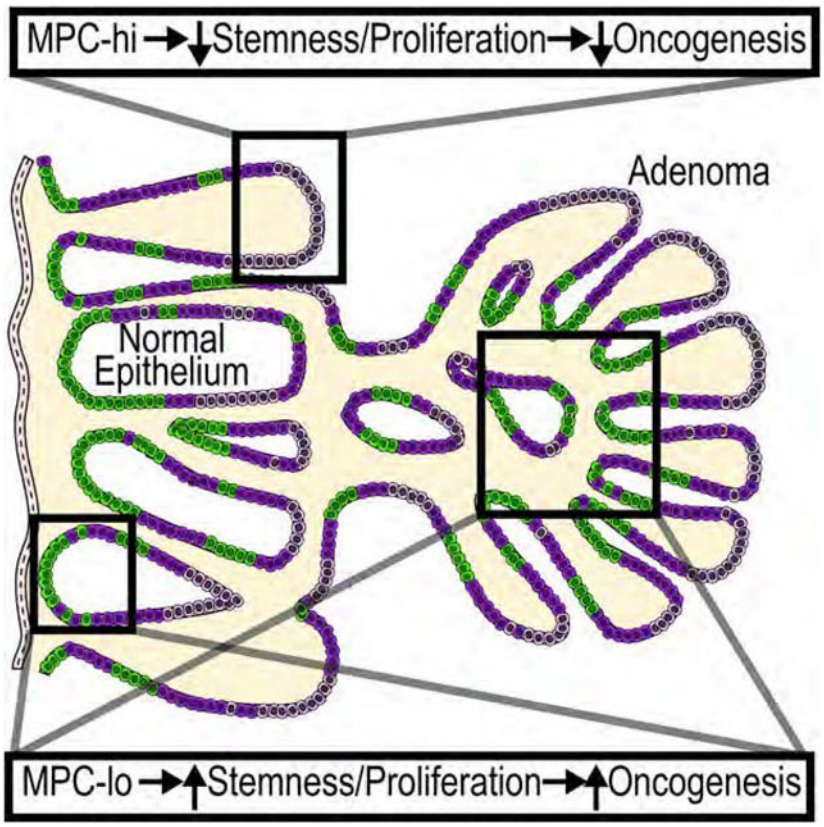

eTOC Blurb

A hallmark of cancer is altered metabolism in tumor cells, however, it is unclear whether cancer initiation also requires metabolic changes. Bensard, et al. demonstrate that constitutive enforcement of a glycolytic program through inactivation of the Mitochondrial Pyruvate Carrier (MPC), is necessary and sufficient to drive intestinal tumor formation.

Introduction

It is now nearly universally accepted that cancers exhibit a metabolic state that enables the tumor to build the biomass necessary for continuous proliferation, particularly in a microenvironment with limited oxygen and metabolites due to poor vascularization (Pavlova and Thompson, 2016; Vander Heiden and DeBerardinis, 2017). Indeed, it has been typically

assumed that these metabolic phenotypes are adaptations to the unique requirements of the tumor microenvironment (Olson et al., 2016; Samanta and Semenza, 2018; Xie and Simon, 2017). Moreover, the atypical metabolic program of cancer cells is essential for tumor establishment and maintenance in animal models and is therefore the target of most metabolic experimental therapeutics (Bader et al., 2019; Hong et al., 2016; Schell et al., 2014; Sullivan et al., 2015; Yang et al., 2014). However, our understanding of cancer metabolism has been largely based on experiments comparing normal tissue to established tumors or cells derived from those tumors. In contrast, we have relatively little understanding of the metabolic underpinnings of tumor initiation.

If these metabolic "adaptations" are selected as a result of the constraints of the environment found in an established tumor, then one might hypothesize that they should only become prevalent or important well after the initial hyperproliferative events in tumor initiation. We set out to test this hypothesis by analyzing whether tumor initiation might also be subject to specific metabolic requirements and/or drivers using colon cancer as a model. Sporadic colon tumors are believed to follow a stereotypical progression wherein the initial tumorigenic event triggers intestinal stem cell hyperplasia, which leads to the formation of a benign adenoma (Sohaily et al., 2012; Vogelstein et al., 2010). This initial event is associated with hyperactivation of the Wnt/β-catenin pathway, typically through loss of function of the *Apc* tumor suppressor (Nusse and Clevers, 2017). Roles for Apc are conserved through evolution, with *Apc* mutations in *Drosophila* leading to increased intestinal stem cell proliferation and intestinal hyperplasia, similar to that seen in mammals (Cordero et al., 2012; Lee et al., 2009). Eventually, additional tumorigenic insults lead to the progression of this lesion into an invasive adenocarcinoma, which results in morbidity and mortality in human patients (Marley and Nan, 2016; Weinberg and Marshall, 2019).

Our studies found that the earliest transition, from normal human intestinal epithelium to a hyperplastic adenoma, is associated with a gene expression pattern that corresponds to an aerobic glycolytic metabolic program with low mitochondrial carbohydrate oxidation. To test the impact of this metabolic program in tumor initiation, we employed genetic manipulation of the Mitochondrial Pyruvate Carrier (MPC) as a means of modulating glucose metabolism in *Drosophila* and mice. The MPC is an evolutionarily conserved obligate heterodimer of two proteins, MPC1 and MPC2, that resides in the inner mitochondrial membrane and transports pyruvate into the mitochondrial matrix for oxidative metabolism (Bricker et al., 2012; Herzig et al., 2012). Consistent with this, the MPC is frequently deleted or under-expressed in many forms of cancer and re-expression of the MPC in colon cancer cells is sufficient to reduce their growth rate and tumorigenicity in mouse models (Rauckhorst and Taylor, 2016; Schell et al., 2014). We found that overexpression of the MPC is sufficient to fully block proliferation in intestinal stem cells that lack either Apc or Notch tumor suppressors. A similar effect is seen upon disrupting lactate dehydrogenase (LDH) function in oncogenic intestinal stem cells indicating that Apc-mediated tumor formation requires an appropriate cellular metabolic context. We also generated animals wherein intestinal stem cells are deleted for the MPC and, therefore, have a constitutively glycolytic metabolic program (Bricker et al., 2012; Herzig et al., 2012; Schell and Rutter, 2013). In multiple models of *de novo* tumor initiation, this manipulation was sufficient to significantly increase the frequency of adenoma formation and to result in

the formation of higher-grade adenomas. This phenotype was accompanied by increased expression of canonical markers of Wnt/β-catenin signaling, suggesting that this pathway contributes to tumor formation. Our data suggest that a glycolytic metabolic program supports the initial steps of tumorigenesis, likely by driving a pro-proliferative gene expression program, establishing metabolism as a gatekeeper for intestinal tumor initiation.

Results

Modulating pyruvate metabolism predicts and predisposes for colon adenoma formation

In an effort to define the metabolic program that characterizes early colon adenomas, we interrogated two gene expression datasets generated from early stage human adenomas compared to normal colon (Sabates-Bellver et al., 2007; Skrzypczak et al., 2010). This analysis revealed robust differences in gene expression, including alterations in genes that control glucose metabolism (Figure S1A–B, Berg 2019). Lactate Dehydrogenase (LDH), which is required for the conversion of the glycolytic product pyruvate to lactate, was expressed more highly in adenomas (Figure 1A and S1C). This is consistent with the known role of LDH in diverting carbohydrate metabolites away from mitochondrial import and oxidation as part of aerobic glycolysis, which is often observed in established tumors and cells derived therefrom (Romero-Garcia et al., 2016; Sun et al., 2017; Vander Heiden et al., 2009). In contrast, we found that the genes that encode the first step in the oxidation of pyruvate, mitochondrial import, mediated by the Mitochondrial Pyruvate Carrier (MPC - encoded by the *Mpc1* and *Mpc2* genes) were both decreased in expression in adenomas (Figure 1B and S1D). Human colon adenocarcinomas, from TCGA and the above studies, also exhibit increased expression of *LDHA* and *LDHB* and decreased expression of *MPC1* and *MPC2*, as previously observed (Schell et al., 2014) (Figure 1A, 1B, S1E). The fact that this gene expression phenotype is recapitulated in early stage adenomas implies that this transcriptional regulation of pyruvate metabolism might occur earlier than the establishment of an ischemic tumor microenvironment. We also found that the expression of both *Mpc1* and *Mpc2* are decreased in adenomas derived from two distinct mouse models of colon cancer, the azoxymethane/dextran sodium sulfate (AOM-DSS) model and a genetic model of heterozygous loss of *Apc* in intestinal stem cells (Figure 1C, 1D). This decreased expression is also observed at the level of protein abundance (Figure 2D, 3D).

Although we recognize that the phenotype of the established lesion, even if it is as early as the adenomas described, is not necessarily tied to the initial events of tumorigenesis, these data are consistent with the notion that tumor initiation is associated with the establishment of an aerobic glycolytic metabolic program with limited mitochondrial pyruvate uptake and oxidation. Therefore, we sought to test the hypothesis that constitutive enforcement of this metabolic program in normal intestinal stem cells might predispose those cells for hyperproliferation and adenoma formation. To do so, we employed a mouse model wherein we deleted *Mpc1* selectively in adult LRIG1$^+$ intestinal stem cells (*Mpc1*^{Lrig1KO}) (Figure S1F) (Powell et al., 2012). This approach is sufficient to cause loss of MPC1 and MPC2 proteins, due to their co-dependence for protein stability, and complete ablation of MPC activity (Flores et al., 2017; Gray et al., 2015; Grenell et al., 2019; Rauckhorst et al., 2017; Schell et al., 2017). Three consecutive days of tamoxifen injection led to a near complete

loss of *Mpc1* mRNA and MPC1 protein across the GI tract (Figure 1D–E). Otherwise untreated $Mpc1^{Lrig1KO}$ mice exhibited overtly normal small intestine and colon morphology and length as well as unchanged body weight, body composition, food/water intake, metabolic rate, locomotor activity and intestinal barrier function at 120 days post-recombination (Figure S1G–M).

This genetic model was then subjected to an AOM-DSS treatment in order to elicit a tumorigenic environment (Figure 1C). Control mice exhibited a modest macroscopic tumor burden, with 55% of mice having fewer than 3 adenomas and only 10% having more than 5 adenomas at 100 days post-AOM (Figure 1F). In contrast, $Mpc1^{Lrig1KO}$ mice exhibited an increased tumor burden compared to controls, with only 15% having fewer than 3 lesions and 60% having more than 5 (Figure 1F). To complement the environmental tumor model described above, we employed two genetic $Apc^{flox/+}$ models, one originating in the adult LRIG1+ intestinal stem cells ($Apc^{Lrig1KO/+}$) and a second targeting the entire Villin+ intestinal epithelium ($Apc^{VillKO/+}$) (Figure 1C) (Colnot et al., 2004; Marjou et al., 2004; Powell et al., 2014; Powell et al., 2012). In both models, tumor formation was elicited by sporadic loss of *Apc* heterozygosity after tamoxifen-induced inactivation of one allele (Barker et al., 2009; Beyaz et al., 2016; Colnot et al., 2004; Powell et al., 2014; Powell et al., 2012). Consistent with previous reports, $Apc^{Lrig1KO/+}$ mice exhibited a modest macroscopic tumor burden assessed from the duodenum to rectum, with 60% of mice having fewer than 10 adenomas and none having more than 24 at 90 days post-TAM (Figure 1G). The $Apc^{Lrig1KO/+}Mpc1^{Lrig1KO}$ mice exhibited a higher tumor burden, with only 18% having fewer than 10 lesions and 45% having more than 25 (Figure 1G). Similarly, $Apc^{VillKO/+}$ mice exhibited a modest macroscopic tumor burden, with 72% of mice having fewer than 10 adenomas and only one mouse having more than 25 at 140 days post-TAM (Figure 1H). Homozygous loss of *Mpc1* ($Apc^{VillKO/+}Mpc1^{VillKO}$) increased tumor burden dramatically such that only 44% had fewer than 10 lesions and 51% had more than 25 (Figure 1H). Interestingly, *Mpc1* loss was associated with cellular hyperproliferation in the crypt at multiple timepoints in each of these models, despite otherwise normal crypt morphology and apoptosis (Figure S1N–S). In each of these analyses, heterozygous mice exhibited an intermediate phenotype. Apoptosis was unaffected by *Mpc1* loss, with apoptotic events being restricted to the luminal surface of the colon, as expected (Figure S1T). These data demonstrate that a loss of MPC function and the concomitant impairment of mitochondrial pyruvate uptake is sufficient to promote intestinal tumor initiation in the background of multiple mouse cancer models.

Loss of *Mpc1* promotes tumor initiation in an environmental tumor model

$Mpc1^{Lrig1KO}$ mice exhibited a substantial increase in the incidence of macroscopic tumors compared to controls in the AOM-DSS experiment (Figure 2A). There was not a consistent gene dose-dependent difference in adenoma size across all genotypes (Figure S2A). The increased adenoma incidence was observed along the length of the colon, but was most pronounced in the proximal colon (15%, 12.8%, and 25.3% proximal distribution in control, $Mpc1^{Lrig1KO/+}$, and $Mpc1^{Lrig1KO}$ respectively; Chi-square test p=0.0592) (Rosenberg et al., 2009). All genotypes exhibited a similar extent of AOM-induced DNA damage as assessed by quantifying nuclear positivity of phospho-histone H2A.X (Figure S2B). Moreover, the

body weight response to DSS-induced colitis, body composition, and intestine length were similar across all genotypes (Figure S2C–E), suggesting that the observed tumor phenotype is unlikely to be the result of experimental or systemic parameters.

Colons from the AOM-DSS-treated mice were subjected to blinded histological examination. As expected from the macroscopic examination, $Mpc1^{Lrig1KO}$ exhibited a higher overall tumor burden (Figure 2B, S2F). Whereas control mice developed only low-grade adenomas with limited focal high-grade features, loss of *Mpc1* led to robust high-grade lesions, as noted histologically by fulminant crypt necrosis (shown) and cribriform glands (not shown) (Figure 2BC). This was particularly true upon homozygous *Mpc1* deletion (Figure 2B). As expected, MPC1 protein was absent in $Mpc1^{Lrig1KO}$ adenomas and this led to loss of MPC2 protein as previously observed (Figure 2D) (Schell et al., 2017; Gray et al., 2015). Consistent with our mRNA analyses, MPC1 protein expression was present in control adenomas, though strongly reduced compared to adjacent normal tissue (Figure 2D). $Mpc1^{Lrig1KO}$ adenomas exhibited increased cellular proliferation, as assessed by increased Ki67 staining in grade-matched histological sections (Figure 2E), but no change in the frequency of apoptosis, as assessed by cleaved Caspase-3 positive nuclei staining (Figure 2F). While examination at 100 days post-AOM is typical in the AOM-DSS model, and the resulting data were supportive of the hypothesis that loss of *Mpc1* led to accelerated tumor initiation, we also wanted to perform an earlier examination to capture the initial signs of adenoma formation. We therefore sacrificed mice at 49 days post-AOM and performed a histological analysis similar to that depicted in Figure 2C. At this time point, $Mpc1^{Lrig1KO}$ and control colon epithelium showed similar residual epithelial injury and active inflammation, which is consistent with them having a similar direct response to the inflammatory and mutagenic burden (see Figure S2B–C). However, signs of hyperproliferative lesions, in the form of more and larger aberrant epithelial foci, were observed in $Mpc1^{Lrig1KO}$ mice (Figure 2G, S2G). These data suggest that the higher grade of adenomas in the $Mpc1^{Lrig1KO}$ mice at 100 days is unlikely to be explained simply by more rapid progression, and perhaps more importantly, that the earliest indicators of future tumor formation were more frequent upon *Mpc1* deletion. Most likely, this is indicative of *Mpc1* deletion rendering a higher number of cells susceptible to tumor initiation.

Loss of *Mpc1* promotes tumor initiation in genetic tumor model

Unlike the AOM-DSS model, wherein adenomas were restricted to the proximal and distal colon, the $Apc^{Lrig1KO}$ model exhibited adenomas throughout the small intestine and colon (Beyaz et al., 2016; Colnot et al., 2004; Johnson and Fleet, 2012). While the macroscopic tumor burden was much higher upon loss of *Mpc1*, the distribution of lesion site was not significantly different (p=0.0767) (Figure 3A and S3A–B). Blinded pathological grading of tumor histology showed a dramatic increase in the number of <1mm microadenomas in $Apc^{Lrig1KO/+}$ $Mpc1^{Lrig1KO}$ intestine and colon as well as larger (>1mm) adenomas (Figure 3B). The lesions were almost exclusively low-grade dysplasia in both genotypes, although we observed rare high-grade lesions exclusively in the *Mpc1*-deficient setting (Figure 3B). All dysplastic lesions demonstrated nuclear β-catenin at multiple locations, which is consistent with complete loss of *Apc* function (Figure 3C). As with the AOM-DSS model, MPC1 protein (and MPC2 protein as a result) was absent in $Mpc1^{Lrig1KO}$ adenomas and was

decreased relative to adjacent normal tissue in control adenomas (Figure 3D). Similar to the AOM-DSS model, we observed no consistent gene dosage-effect of MPC loss on tumor size, intestine length, or body weight during the experiment (Figure S3C–E). In contrast, unlike the AOM-DSS model, loss of *Mpc1* was not associated with increased intra-adenoma proliferation in the $Apc^{Lrig1KO}$ model, as assessed by quantification of Ki67 staining (Figure 3E), consistent with the similar tumor sizes and grades across *Mpc1* genotypes in this model. *MPC1* genetic status had no effect on the incidence of apoptosis, as assessed by cleaved Caspase-3 positive nuclei staining in grade-matched histological sections (Figure 3F). The similarity between genotypes in tumor grade and proliferation in the *Apc* loss-driven tumor model, unlike that observed in the AOM-DSS model, raises the possibility of a genetic relationship between *Mpc1* and *Apc* in tumor phenotype, which is discussed in more detail below.

To complement the above experiment using the *Lrig1-CreER* knock-in allele and to ensure that the observed phenotypes are not related to any peculiarities of this Cre driver (Powell et al., 2012), we performed a similar study of *Apc* and *Mpc1* deletion employing tamoxifen-inducible Cre recombinase under control of the *Villin* promoter ($Apc^{VillKO/+}Mpc1^{VillKO}$) (Figure 1C) (Marjou et al., 2004). Gross assessment again confirmed that $Apc^{VillKO/+}Mpc1^{VillKO}$ mice had higher tumor burden compared to $Apc^{VillKO/+}$ mice, and this was found throughout the intestine and colon (Figure 3G and S3F–G). As in the *Lrig1-CreER* model, adenoma size was not affected between *Mpc1* genotypes nor was intestine length or body weight (Figure S3H–J). Histological examination revealed that, again, adenomas were almost exclusively low-grade regardless of *Mpc1* genotype (Figure 3H). The increased proportion of low-grade microadenomas (<1mm) in $Apc^{VillKO/+}Mpc1^{VillKO}$ mice reinforced the hypothesis that upon *Apc* inactivation, the loss of *Mpc1* does not markedly affect tumor size or progression and that these two genes might share a specific genetic relationship (Dow et al., 2015; Sandoval et al., 2017; Schell et al., 2017).

Apc mutant tumor expansion in *Drosophila* is not affected by loss of mitochondrial pyruvate import

Our studies of MPC function in mouse adenoma formation depend on the clonal expansion of cells that undergo sporadic tumorigenic mutations in the AOM-DSS model or sporadic loss of the wild-type allele in the $Apc^{Lrig1KO/+}$ model. To confirm and extend this mammalian genetic approach, we turned to genetic manipulations in the *Drosophila* intestinal stem cell lineage where we can engineer a homozygous loss of *Apc* function in single stem cells in either the presence or absence of the MPC. As in mammals, the *Drosophila* intestinal epithelium is maintained by regulated intestinal stem cell proliferation and differentiation (Micchelli and Perrimon, 2006; Ohlstein and Spradling, 2006). Our studies use MARCM clonal analysis to disrupt gene function in single intestinal stem cells and follow subsequent clonal expansion using a GFP lineage marker (Figure S4A) (Wu and Luo, 2006). In previous work, we showed that a loss of *MPC* function led to a two-fold increase in the size of *Drosophila* intestinal clones lacking *Notch* signaling, indicating that the MPC normally suppresses Notch enteroendocrine tumor expansion (Schell et al., 2017). To determine if a similar effect is seen on Apc tumor growth, we used MARCM clonal analysis to disrupt *MPC* function in intestinal stem cells that carry mutations in the two

Drosophila Apc genes (Cordero et al., 2012; Lee et al., 2009). As expected, mutant clones lacking both *Apc1* and *Apc2* function are significantly larger than wild-type clones (Figure 4A, 4D, 4F) or clones that lack *MPC* function (Figure 4B, 4C, 4F). The size of *Apc* mutant clones, however, is unaffected by a loss of the MPC (Figure 4E, 4F). This result parallels that described previously in $Apc^{Lrig1KO/+}$ mice in which adenoma size is not affected by a loss of MPC function, suggesting that the interplay between pyruvate metabolism and Apc-mediated tumor initiation is conserved through evolution. In addition, these studies suggest that, unlike the case with *Notch* loss of function, *Apc* mutant tumors appear to be operating at a maximal glycolytic capacity that cannot be further enhanced by changes in mitochondrial pyruvate metabolism.

Ectopically increased mitochondrial pyruvate metabolism blocks tumor formation

Overexpression of *Mpc1* and *Mpc2* is sufficient to reduce normal intestinal stem cell proliferation rates in *Drosophila* and increase mitochondrial pyruvate oxidation and proliferation in cancer cell lines (Schell et al., 2014; Schell et al., 2017). We thus exploited this genetic tool by engineering *Drosophila* intestinal stem cells that lack key tumor suppressors in either the absence or presence of *MPC* overexpression. This allows us to study the impact of increased mitochondrial pyruvate import at the earliest steps of oncogenesis. Accordingly, we examined the effect of *dMpc1* and *dMpc2* overexpression on the expansion of intestinal stem cells that lack *Apc* function. As expected, *Apc* mutant MARCM clones grow to more than twice the size of wild-type clones by five days after clone induction (Figure 4G, 4H, 4K). Intestinal stem cells that overexpress the *MPC* have reduced proliferation, consistent with our earlier observations (Figure 4I) (Schell et al., 2017). However, in contrast to the somewhat smaller *Apc* mutant clones that we expected to see upon *MPC* overexpression, we found a complete block in *Apc* clonal expansion under these conditions (Figure 4J, 4K). Antibody stains confirmed that these cells overexpress the MPC as expected (Figure S4B). Importantly, the same effect is also seen at twenty days after clone induction (Figure 4L–P). In addition, the number of *Apc* mutant clones with *MPC* overexpression does not change in intestines between five and twenty days demonstrating that *MPC* overexpressing cells are not more likely to undergo cell death (Figure S4C). Taken together, these results demonstrate that *MPC* overexpression does not affect the lifespan of the cells in which it is expressed, but it is sufficient to block the oncogenic effects of *Apc* loss-of-function.

The block in proliferation mediated by *Apc* loss might be due to a property of *MPC* overexpression other than its effect on metabolism. To test this possibility, we directed RNAi against *LDH* in *Apc* mutant clones. Reduced *LDH* activity leads to decreased aerobic glycolysis and increased mitochondrial oxidative metabolism in cancer cells (Fantin et al., 2006; Li et al., 2017; Schell et al., 2017; Xie et al., 2014). Consistent with these activities, expression of *LDH* RNAi in *Apc* mutant clones severely reduced their expansion, similar to the block in proliferation seen upon *MPC* overexpression (Figure 5A–E). Taken together with our studies of the MPC, these observations indicate that cellular metabolism acts downstream of the oncogenic pathways that are unleashed by *Apc* mutations in intestinal stem cells. Interestingly, this genetic placement is consistent with studies in zebrafish, which

have shown that the *MPC* acts downstream from *Apc* in its roles in heart and intestinal development (Sandoval et al., 2017).

A loss of *Notch* signaling in intestinal stem cells results in a distinct type of tissue overgrowth in the intestine relative to *Apc* mutations, characterized by a restriction of the differentiated cell fate to the enteroendocrine (EE) lineage (Ohlstein and Spradling, 2006, 2007). We thus examined the effect of MPC overexpression on intestinal stem cells that lack *Notch* in an effort to determine if the resulting shift in metabolism is sufficient to block other types of intestinal hyperproliferative lesions. As expected, targeting *Notch* RNAi to intestinal stem cells results in significant clonal overgrowth (Figure 5F). This growth, however, is completely blocked by either *MPC* overexpression (Figure 5G, 5I) or *LDH* RNAi (Figure 5H, 5I), similar to our observations of *Apc* mutant clones. In addition, clones that lack *Notch* function in the presence of either *MPC* overexpression or *LDH* RNAi fail to stain for the Prospero marker for EE cells, indicating that these cells do not differentiate along the EE lineage as is usually seen in mutant *Notch*-derived tumors (Figure S4D–F). This observation, combined with the small size of the *Notch* RNAi cells, argues that they have maintained their precursor cell fate in spite of *MPC* overexpression or *LDH* RNAi. Taken together, these results suggest that reduced mitochondrial pyruvate metabolism is a common potentiator of hyperproliferation in oncogenic intestinal stem cell models in *Drosophila*.

MPC-mediated mitochondrial pyruvate oxidation is limited in intestinal stem cells and tumors

We returned to the mouse model to better characterize the metabolic consequences of MPC manipulation. To measure the contribution of glucose to the metabolic flux of intestinal crypt cells, we isolated crypts from control or $Mpc1^{VillKO}$ mice and incubated them with ^{13}C-glucose immediately *ex vivo*, followed by metabolite extraction and both GC- and LC-MS analysis. As expected, $Mpc1^{VillKO}$ did not affect glucose uptake or glycolytic production of pyruvate (Figure 6A). However, despite this strong pyruvate labeling, little glucose carbon entered the TCA cycle in control crypts (Figure 6B). The direct labeling of representative TCA cycle intermediates citrate and malate and the TCA cycle derivative aspartate from ^{13}C-pyruvate (the M+2 isotopomers of citrate, malate and aspartate) was between 5 and 15%. In $Mpc1^{VillKO}$ crypts, this limited labeling from ^{13}C-glucose into TCA metabolites was significantly reduced, consistent with a severe decrease in mitochondrial pyruvate uptake (Figure 6B). These data implied that other substrates might preferentially contribute carbon to the TCA cycle in intestinal crypts. We therefore set out to conduct analogous metabolic labeling experiments with ^{13}C-labeled palmitate and glutamine. Exogenous palmitate is not typically added directly to cells in culture, beyond what is provided from serum. Therefore, before the palmitate tracing experiment, we assessed whether the addition of palmitate would significantly alter glucose contribution to the TCA cycle. Freshly isolated crypts were incubated with ^{13}C-glucose and delipidated BSA with and without added palmitate. The contribution of glucose to mitochondrial TCA intermediates was similar between the two conditions, suggesting that the added palmitate did not significantly affect the flux of glucose oxidation (Figure S5A). We therefore conducted all isotope labeling

experiments, including those with ^{13}C glucose (Figure 6A, 6B), in the presence of delipidated BSA with palmitate.

We found that unlike glucose, both glutamine and palmitate contributed significantly to TCA cycle intermediates (Figure 6C, S5B). The contribution of ^{13}C-glutamine was similar between control and *Mpc1*^{VillKO} crypts (Figure S5B). In contrast, ^{13}C-palmitate labeling into TCA cycle intermediates citrate and malate was significantly increased in the *Mpc1*^{VillKO} crypts (Figure 6C). To quantify the specific contribution of the labeled nutrients to TCA metabolism, we calculated the normalized labeling fraction of each input towards either citrate or malate (Buescher et al. 2015). The palmitate labeling contribution increased to such a degree as to fully compensate for the loss of glucose flux into the TCA cycle in *Mpc1*^{VillKO} crypts (Figure 6D).

Considering that fully formed tumors might have a different metabolic profile than the stem cell-enriched crypts from which they arose, we isolated adenomas from *Apc*$^{Lrig1KO/+}$ and *Apc*$^{Lrig1KO/+}$ *Mpc1*^{Lrig1KO} mice at 90 days post-recombination and performed an immediate *ex vivo* isotope labeling experiment analogous to those described above for intestinal crypts. In the adenomas derived from *Apc*$^{Lrig1KO/+}$ animals, glucose, palmitate and glutamine all contributed to citrate, with glutamine being the dominant contributor to malate (Figure 6E). Interestingly, while labeling with ^{13}C-glucose led to robust (~60%) labeling of the pyruvate pool as observed in the crypts (Figure 6F), labeling with ^{13}C-glutamine led to a limited (~15%) labeling of the glutamate pool (Figure S5C), implying that glutamine contribution to the TCA cycle is much larger than depicted in the unnormalized measurements shown in Figure 6E. Glucose contribution to citrate labeling was diminished in adenomas from *Apc*$^{Lrig1KO/+}$ *Mpc1*^{Lrig1KO} mice. Unlike *Mpc1*-deficient crypts, however, the glucose-deficient labeling was not made up by increased palmitate-derived citrate. Instead, 13C-glutamine contribution to citrate was profoundly increased in adenomas derived from *Apc*$^{Lrig1KO/+}$ *Mpc1*^{Lrig1KO} mice (Figure 6E and S5D).

MPC loss elicits a more stem cell-like gene expression pattern in tumors

To begin to elucidate the mechanism underlying the effect of *Mpc1* deletion on tumor initiation, we transcriptionally profiled size and grade-matched adenomas and adjacent normal tissue from AOM-DSS-treated and *Apc*$^{Lrig1KO/+}$ mice using a custom NanoString gene panel (Figure 7A, 7B, Berg 2019; Merlos-Suárez et al., 2011; Nusse and Clevers, 2017; Schell et al., 2017). We found that the adjacent normal tissue exhibited low expression of stem cell markers and high expression of differentiation markers in both models (Figure 7A, 7B: red and green). Interestingly, adenomas from control AOM-DSS mice clustered in distinct groups based upon the expression of stemness and differentiation marker genes. A subset of adenomas showed a similar pattern of gene expression to normal tissue (Figure 7A: orange with red bracket). The remainder of control adenomas displayed a more variable gene expression pattern, but was distinctly more similar to stem cells (Figure 7A: orange). Interestingly, every adenoma from *Mpc1*^{Lrig1KO} mice clustered with the stem-like group of control adenomas (Figure 7B: blue). This suggests that transformation and adenoma formation in control mice might be heterogeneous, resulting in both more differentiated lesions or more stem-like lesions. In contrast, the metabolic consequences of MPC loss

resulted in all *Mpc1*^{Lrig1KO} adenomas attaining the more stem-like phenotype. Interestingly, adenomas from the *Apc*$^{Lrig1KO/+}$ model did not exhibit this *Mpc1* genotype effect (Figure 7B). All adenomas clustered distinctly from the adjacent normal tissue, being characterized by enhanced expression of stemness markers, with no difference between *Apc*$^{Lrig1KO/+}$ and *Apc*$^{Lrig1KO/+}$ *Mpc1*^{Lrig1KO} mice (Figure 7B). This is consistent with the fact that all adenomas in the *Apc*$^{Lrig1KO/+}$ model result from the homozygous loss of *Apc* and constitutive activation of the pro-stemness Wnt/β-catenin pathway, which appears non-additive with the prostemness metabolic consequences of MPC loss. Once *Apc* is lost, there appears to be no additional impact of MPC loss on the stemness gene expression program, which is consistent with previous results employing pharmacological modulators of the Wnt/β-catenin pathway and the MPC in intestinal organoids (Sandoval et al., 2017; Schell et al., 2017; van der Flier and Clevers, 2009).

To interrogate the relevance of our findings in mouse models to human colon cancer, we queried two datasets that contain normal and adenoma samples (Sabates-Bellver et al., 2007; Skrzypczak et al., 2010). As described previously, we found that *Mpc1* and *Mpc2* gene expression was lower in adenomas compared to normal human colon (see Figure 1B and S1D). As with our murine studies, we found that expression of the same panel of stemness and differentiation genes distinguished normal colon from adenomas in both datasets (Figure S6A–F). We further queried these human datasets for associations between *Mpc1* and *Mpc2* gene expression and all other genes. Filtering with a correlation threshold of $r > 0.6$ and p-value < 0.01, we employed both PANTHER (v13.1) and DAVID (v6.8) tools to identify known pathways that were enriched in genes whose expression correlates with *Mpc1* or *Mpc2* (Berg 2019; Huang et al., 2009a; Huang et al., 2009b; Thomas et al., 2003; Thomas et al., 2006). We found that *Mpc1* expression inversely correlated with several cell proliferation and biosynthetic metabolism pathways, including purine biosynthesis, cell cycle and stem cell regulation (Figure 7C and S6G). Interestingly, both analyses also identified an inverse correlation between *Mpc1* gene expression and the Wnt signaling pathway (Figure 7C and S6G). Upon deeper interrogation, *Mpc1* expression negatively correlated with canonical colonic Wnt/β-catenin target genes, as shown for *Axin2* ($r= -0.73$, p= 1.25E-12), and *Sox9* ($r= -0.67$, p= 3.12E-10), (Figure 7D, S6H–I, Berg 2019; Nusse and Clevers, 2017). This relationship between *Mpc1* gene expression and activity of the Wnt/β-catenin pathway is reminiscent of the mouse adenoma data described above and is suggestive of regulatory interplay between *Mpc1* and the *Apc* repressor of Wnt/β-catenin pathway activity.

Discussion

We set out to characterize the metabolic hallmarks of tumor initiation and determine if they play an instructive role in promoting tumorigenesis (Pavlova and Thompson, 2016). In support of this concept, we found that some of the earliest molecular features of hyperproliferative colon adenomas in both mice and humans are suggestive of a metabolic program of aerobic glycolysis, characterized by low mitochondrial import and oxidation of the glycolytic product pyruvate. Consistent with these correlative data, we found that intestinal crypts, which are rich in intestinal stem cells, the cell of original for colon tumors, exhibit limited glucose contribution to mitochondrial oxidation. Instead, palmitate and glutamine are more significant mitochondrial substrates in these cells. These data led us to

hypothesize that constitutive enforcement of a glycolytic and non-oxidative program of carbohydrate metabolism might predispose these crypt cells, which are believed to be the tumor initiating cells, for tumor initiation in the colon. Using genetic ablation of the Mitochondrial Pyruvate Carrier (MPC), which leads to constitutively impaired mitochondrial pyruvate oxidation, we demonstrated that the establishment of a metabolic program of glycolysis and its derivative pathways is sufficient to promote tumor formation in multiple mouse intestinal cancer models. We also tested the hypothesis that decreased mitochondrial pyruvate oxidation might be required for tumorigenesis. Using two distinct *Drosophila* models of clonal tumorigenic hyperproliferation, we found that constitutive enforcement of high mitochondrial pyruvate import was sufficient to completely block tumor formation.

The mammalian data presented herein are suggestive of a genetic and regulatory relationship between the Wnt/β-catenin pathway, which is critical in maintaining stem cell identity, and mitochondrial pyruvate import and metabolism (Sandoval et al., 2017; Schell et al., 2017). First, as early as we can detect the hyperproliferative lesions resulting from homozygous loss of *Apc* in the $Apc^{Lrig1KO/+}$ model, those lesions exhibit low expression of *Mpc1* and *Mpc2*. These data are consistent with the hypothesis that loss of *Apc* enforces decreased expression of the MPC genes and establishment of a glycolytic metabolic state. Second, we found that activity of the Wnt/β-catenin pathway, as assessed by expression of its target genes, is inversely correlated with *Mpc1* gene expression in human normal and adenomatous colon. Third, while loss of *Mpc1* changes the characteristics of adenomas generated in the sporadic AOM-DSS model, adenomas generated in response to *Apc* loss are essentially identical regardless of *Mpc1* status. This is most clearly demonstrated by comparison of gene expression across *Mpc1* genotypes in the AOM-DSS versus *Apc* deletion models. Control adenomas in the AOM-DSS model exhibit heterogeneity in their expression pattern of stemness and differentiation genes. Loss of *Mpc1* leads to a profound constraint on that heterogeneity, whereby every adenoma clusters in the more “stem-like” group. On the other hand, when tumors are initiated by loss of *Apc*, additional loss of *Mpc1* has no significant effect on expression of these genes. This same concept is recapitulated by analysis of intra-adenoma proliferation. Both loss of *Mpc1* (in the AOM-DSS model) and loss of *Apc* lead to increased cellular proliferation, but combining *Mpc1* loss with the *Apc* model has no additional effect. Similarly, loss of *Mpc1* leads to a striking increase in the frequency of high-grade features in adenomas from the AOM-DSS model. However, in the *Apc* model, adding the genetic deletion of *Mpc1* has essentially no effect. Interestingly, loss of *Mpc1* does increase the frequency of adenoma formation in the *Apc* model, even if those adenomas are not different. We believe that this is best explained by loss of *Mpc1* leading to increased frequency of *Apc* loss of heterozygosity, which is the precipitating genetic lesion for tumorigenesis in this model. Indeed, we observed increased cellular proliferation in normal crypts upon *Mpc1* deletion without a matched increase in apoptosis, which would be predicted to increase the frequency of replication errors that would result in inactivation of the remaining wild-type *Apc* allele (Barker et al., 2009; Dow et al., 2015; Sansom et al., 2007; Tomasetti et al., 2017).

A genetic relationship between *Apc* and *Mpc1* is further supported by our studies in *Drosophila*. As in the mouse, loss of either the MPC or *Apc* leads to hyperproliferation of

Drosophila intestinal stem cells, however, there is no additive effect of combining these genetic disruptions. More importantly, we find that the hyperproliferation elicited by a deletion of *Apc* is completely suppressed by ectopic expression of the MPC. This is reminiscent of a similar effect reported in the zebrafish intestine, wherein MPC1 expression rescues the differentiation defects imposed by a loss of *Apc* (Sandoval et al., 2017). Taken together, the data presented in the mammalian and fly intestine and that from published work in zebrafish support the hypothesis that *Mpc1* is genetically epistatic to *Apc*. In the context of cancer, the MPC thus functions downstream from traditional tumor suppressor genes to regulate tumor initiation and growth.

We propose that the *Mpc1*-dependent effects described herein are explained by a stem cell autonomous mechanism. In *Drosophila*, the MARCM clonal analysis used for our studies effectively targets genetic manipulations to single intestinal stem cells and marks their lineage. Similarly, in the mouse, we see no evidence, either in the intestine or elsewhere, of a defect that would elicit signaling to intestinal stem cells to promote their hyperplasia or transformation. Moreover, we observe basal hyperproliferation of intestinal stem cells in the context of an otherwise completely normal intestinal epithelium. This is consistent with the previously published observation that low activity of the MPC in intestinal stem cells is critical for maintaining the markers and phenotypes of stemness, including in the simplified *ex vivo* organoid system where cell non-autonomous effects are minimized (Schell et al., 2017). Altogether, we propose the hypothesis that loss of MPC activity elicits a cell autonomous metabolic program that is pro-stemness and pro-proliferative, perhaps similar to the metabolism enforced by the Wnt/β-catenin pathway, and this metabolic milieu promotes the earliest steps of tumor initiation.

We do not yet know why *Mpc1* loss leads to the observed proliferative and pro-tumorigenic phenotype. Our data, however, strongly suggest that it is related to the blockade of mitochondrial pyruvate oxidation and the concomitant establishment of a constitutive aerobic glycolysis program. Indeed, we demonstrate that loss of *Mpc1* leads to a profound loss of glucose contribution to TCA cycle intermediates in intestinal crypts. In addition to loss and gain-of-function for the MPC, we showed in *Drosophila* that inactivation of lactate dehydrogenase in stem cells is sufficient to replicate the effects of MPC overexpression. In all cases, our results were consistent with the metabolic fate of pyruvate playing a decisive role in setting the proliferative tone of intestinal stem cells. These effects of perturbed carbohydrate metabolism are analogous to the observation that increased fatty acid availability and metabolism via a high-fat diet leads to enhanced proliferation and tumorigenesis (Beyaz et al., 2016). Carbohydrate and fatty acid oxidation have a well-described antagonistic relationship and it has been repeatedly observed that loss of MPC activity (and carbohydrate oxidation) leads to increased fatty acid oxidation and vice versa (Goetzman and Prochownik, 2018; Hue and Taegtmeyer, 2009; Schell et al., 2017). Indeed, we found that loss of the MPC in intestinal crypts leads to increased palmitate contribution to TCA cycle flux in *ex vivo* intestinal crypts. It is therefore likely that the published effects of fatty acid abundance and the effects of altered carbohydrate metabolism described herein are two manifestations of a common underlying mechanism (Cheng et al., 2019; Mihaylova et al., 2018). For example, it is possible that loss of *Mpc1* increases tumorigenesis via increased fatty acid uptake and metabolism (Beyaz et al., 2016). Interestingly, we find that

ex vivo adenomas also have limited glucose contribution to TCA cycle intermediates, with the majority being derived from glutamine. Moreover, unlike *Mpc1*-deficient crypts, adenomas from *Mpc1*-deficient mice appear to compensate for the loss of glucose-derived TCA cycle flux by increased glutamine oxidation as seen previously in cultured cancer cells (Yang et al., 2014).

The above data demonstrate that decreased mitochondrial pyruvate metabolism, enforced by elimination of MPC activity, is sufficient to increase the oncogenic susceptibility of the fly and mouse intestinal tract. Therefore, constitutive enforcement in intestinal stem cells of the metabolic program found in hyperproliferative colonic lesions predisposes those stem cells to adenoma formation. Conversely, prevention of that metabolic program prevents proliferation caused by the loss of two distinct tumor suppressors. “Driver” mutations in oncogenes or tumor suppressors have traditionally been thought to be sufficient to direct cell transformation and tumor initiation (Hanahan and Weinberg, 2011; Vogelstein and Kinzler, 2015). In this view, cellular metabolism is seen as providing an important permissive environment that generates the metabolic intermediates required for cell growth and proliferation. Our studies place metabolism in a different context – as a critical gatekeeper that acts downstream from oncogenic signal to drive cancerous initiation and growth.

Limitations of the Study

The most obvious limitation of this study is that the tumor models that we have used are not faithful representations of the typical process of tumor formation in humans. We have used genetic manipulations or treatment with chemical carcinogens to induce tumor formation in mice and flies. While these manipulations are the best available tools for tumor formation in animal models that are broadly accessible, they generate a scenario where essentially all animals exhibit tumor formation within a relatively short timeframe. Future studies will likely address the degree to which a change in cellular metabolic profile predisposes it for tumor formation in more natural settings.

STAR METHODS

LEAD CONTACT AND MATERIALS AVAILABILITY

Further information and requests for resources and reagents should be directed to and will be fulfilled by the Lead Contact, Jared Rutter (rutter@biochem.utah.edu). All unique/stable reagents generated in this study are available from the Lead Contact without restriction.

EXPERIMENTAL MODEL AND SUBJECT DETAILS

Animal Care: All IACUC guidelines were followed and the protocol for mouse experiments carried out in this study was submitted to the University of Utah Institutional Animal Care and Use Committee. Mice were maintained on a Teklad global soy-protein free diet (2920×030917M). Home cages with pelleted paper bedding with nest building enrichment of irradiated paper and tissue strips were placed on ventilated racks with automated water taps. Food and water were available *ad libitum*, and food was only withdrawn if required for an experiment. Mice were co-housed with at least one to four other mice when possible in a temperature-controlled facility with 12-hour light/dark cycles. Mice

were checked daily by facility technicians for signs of distress and bedding changes occurred bimonthly. No formal randomization was performed for mouse studies. Mice were used as they became available, paired with littermate controls where possible. Male and female mice C57BL6J at 8–12 weeks of age were used, and both genders were included in each analysis, except for the metabolic cage measurements in which only male littermates were used to avoid differences due to dyssynchronous estrus cycles. Heterozygous *Lrig1*^{CreER} mice were obtained from Jackson Labs (Powell et al. 2012). *Mpc1*$^{flox/flox}$ mice were generated as previously described (Schell et al. 2017). *Apc*$^{loxp\ exon\ 14}$ (*Apc*$^{flox/+}$) have been described and were a gift from Ömer Yilmaz (MIT) (Beyaz et al. 2016; Powell et al. 2014; Colnot et al. 2004). *Villin*^{CreER} mice were also gifted from Ömer Yilmaz (MIT).

Rodent: Control mice consisted of *Lrig1*^{CreER}and *Mpc1*$^{flox/flox}$ without Cre for chemical carcinogenesis and homeostatic experiments and are combined under the name “Control”. *Lrig1*^{CreER} X *Apc*$^{flox/+}$ (*Apc*$^{Lrig1KO/+}$) and *Villin*^{CreER} X *Apc*$^{flox/+}$ (*Apc*$^{VillKO/+}$) were control mice for genetic carcinogenesis experiments. Breeding lines were maintained and outcrossed Mice in carcinogenesis protocols were inspected daily by lab personnel and weighed at a minimum once a week. Mice showing signs of distress including overgrooming-related sores, weight loss greater than 20% of starting body weight, anal prolapse or frank rectal bleeding were removed from the study and not included in any subsequent final data analyses. The total number of animals removed was 11 animals (7 males, 4 females) with no significance towards genotype or tumor induction model. All compounds used for mouse studies are detail in KEY RESOURCES TABLE. All male and female mice were treated at 8 to 12-weeks of age, receiving three intraperitoneal injections of tamoxifen,100μL 20mg/mL in peanut oil on consecutive days in the mornings between 7:00AM and 11:00AM in home cages.

Colon and Small Intestinal Crypts: Small intestinal and colon crypts were isolated as similarly as described previously (Schell et al. 2017). Mice were euthanized by cervical dislocation, and then gastrointestinal tract dissected from pylorus to anus. The mesentery was removed with scissors. The entire colon and small intestine were opened longitudinally with ball-tip scissors and washed with ice cold PBS. Mucus, fecal remnants, and small intestinal villus were scraped away using a glass coverslip. At this stage, gross specimens for preservation were fixed in buffered 10% formalin (Fisher Scientific 23-245-685) for 24 h, transferred to 70% ethanol and paraffin-embedded for sectioning and staining. Alternately, specimens for crypt isolation were placed in a 2.5mM EDTA-PBS solution incubated at 4°C for 20 minutes with gentle agitation. Tubes were then vigorously shaken by hand 10–20X and the crypt-containing supernatant was transferred into a fresh tube. Crypts were washed in PBS and collected by centrifugation (3 × 300g for 2 minutes at 4°C). At this stage, aliquots were taken and snap frozen in liquid nitrogen for protein analysis or RNA extraction. Viable crypts were resuspended in ice cold DMEM/F12 prior to final resuspension in isotopic labeling media.

***Drosophila* stocks:** *Drosophila* stocks were maintained on standard food containing 3% sucrose, 6% glucose, 8% yeast, and 1% agar in a 25°C incubator. Transgenic lines are as follows: *UAS-dMpc1* RNAi (Bricker et al., 2012), *UAS-LDH* RNAi (VDRC# 102330),

UAS-Notch RNAi (a gift from C. Micchelli), and *UAS-dMpc1-P2A-dMpc2* for *MPC* overexpression (Schell et al., 2017). The *UAS-LDH* RNAi transgenic line has been used previously for functional studies of this enzyme (Charlton-Perkins et al., 2017; Slaninova et al., 2016). A double mutant for $Apc1^{Q8}$ and $Apc2^{N175K}$ was used to remove *Apc* function (Bloomington 7211). A *hs-flp*, *UASGFP*; +; *Tub-GAL4*, *FRT82B*, *TubGal80*/*TM6C* stock (a gift from C. Micchelli) was used to introduce different transgenes and mutants for clonal analysis.

METHOD DETAILS

Characterization of MPC1 deletion in mouse intestine and colon: For experiments relevant to loss of MPC1 in intestinal and colonic homeostasis, 8 to 12-week-old mice were injected intraperitoneally with 100μL of 20mg/mL tamoxifen (Sigma Aldrich T5648) dissolved in peanut oil (Sigma Aldrich P2144) for three successive days and euthanized 30, 60, 90, or 120 days later. BrdU (Invitrogen b23151) was dissolved in PBS (Invitrogen 10010049) to 10mg/mL and 100μL was injected intraperitoneally 4hrs prior to euthanasia to label dividing cells. Injections were carried out in home cages between 7:00AM and 11:00AM and tissue was collected 4-hours later +/−10 min from the time of injection. Dissections of the intestine and colon either were prepared for histological examination or for epithelial collection, described below.

Mouse chemical induction of carcinogenesis: For chemical induction of carcinogenesis (AOM-DSS), control and experimental mice were treated with tamoxifen as described above. 30 days post tamoxifen injection, control and $Mpc1^{Lrig1KO}$ mice were injected with 10mg/mL/kg Azoxymethane (Sigma Aldrich A5486) dissolved in PBS (Invitrogen 10010049). 7 days following AOM injection, mice were subjected to 2% Dextran Sodium Sulfate MW 14000 (USB/Affymetrix 14489) in the facility-provided drinking water for 5 days, followed by facility-provided water for remaining 16 days in a 21-day cycle. Mice underwent 3 cycles of DSS-induced colitis in series. Mice were monitored daily for weight change and removed from the study following greater than 20% body weight loss, extreme diarrhea, or severe rectal bleeding (<5 mice removed total). Mice were euthanized 49 or 100 days following AOM injection. BrdU was administered as described above, though not to the 100 day cohorts. Dissections of the intestine and colon either were prepared for histological examination or for epithelial collection. Tumor burden for tumorigenesis experiments was manually counted using Olympus SZ61 dissecting microscope and imaged via GelDoc Imaging platforms.

Mouse genetic susceptibility to carcinogenesis: For heterozygous *Apc* model of carcinogenesis, control and experimental mice were tamoxifen as described above. $Apc^{Lrig1KO/+}$, $Mpc1^{Lrig1KO/+}Apc^{Lrig1KO/+}$, $Mpc1^{Lrig1KO/}Apc^{Lrig1KO/+}$ mice and $Apc^{VillKO/+}$, $Mpc1^{VillKO/+}Apc^{VillKO/+}$, $Mpc1^{VillKO/}Apc^{VillKO/+}$were monitored every 2–3 days for any signs of intestinal or colonic distress. Mice were euthanized 30, 60, 90, or 140 days ($Apc^{VillKO/+}$ only) following tamoxifen injection. BrdU was administered as described above. Dissections of the intestine and colon either were prepared for histological examination or for epithelial collection. Tumor burden for tumorigenesis experiments was

manually counted using Olympus SZ61 dissecting microscope and imaged via GelDoc Imaging platforms.

Mouse Intestinal Barrier integrity: Control and *Mpc1*^{Lrig1KO} male mice were fasted for 12 hours then gavaged with 100μL/kg fluorescein-isocyannate dextran (FITC-dextran, Sigma Aldrich 46945) dissolved in PBS (background control mice were gavaged with 100μL PBS), and 20μL of corn oil to lubricate the gavage needle in their home cage. Food was then replaced in the cage. 6 hours post-gavage, mice were euthanized and serum obtained via cardiac puncture. The most distal fecal pellet was obtained from the rectum and FITC-dextran extracted via a PBS maceration and centrifugation to clear the debris. Serum and fecal supernatant were diluted 1:10 with sterile deionized water and assayed for fluorescence on Varioskan Flash Spectrophotometer. Background serum and fecal samples were obtained as above to identify background fluorescence from each sample type. All experimental results were analyzed relative to the background adjusted to a value of 1. No subjects or data was excluded from analysis.

Whole mouse body composition and gross metabolism: Control, *Mpc1*$^{Lrig1KO/+}$, and *Mpc1*^{Lrig1KO} male and female mice were weighed once per week beginning with tamoxifen administration. Total body composition was assayed by nuclear magnetic spectroscopy (Bruker MiniSpec) prior to tamoxifen administration and again prior to euthanasia 60 days post tamoxifen and 100 days post azoxymethane. Paired control and *Mpc1*^{Lrig1KO} male littermates were metabolically profiled 60 days post-tamoxifen for 72 hours in metabolic cages. Data from the final full 24 hours was analyzed. All metabolic phenotyping profiles were visualized using Prism GraphPad (v7). Work was performed by the Metabolic Phenotyping Core, a part of the Health Sciences Cores at the University of Utah. No subjects or data was excluded from analysis.

Mouse immunoblotting: Three biological replicate crypt isolations were lysed in RIPA with mammalian protease and phosphatase inhibitors (Sigma Aldrich P8340, Roche Molecular 04906845001). Samples were sonicated and centrifuged at 10,000g for 10 minutes, and the supernatant retained. Protein concentration was determined by BCA Assay (Thermo Scientific 23225) and diluted for equivalent protein loading volumes. Samples were resolved by SDS-PAGE and analyzed by Licor Odyssey. Primary antibodies included MPC1 (Cell Signaling #14462), MPC2 (Cell Signaling #46141), and actin (Millipore MAB1501). Secondary antibodies were Goat Anti-Mouse IgG (H&L) Antibody Dylight™ 800 Conjugated (Rockland #610-145-002-0.5) and Donkey anti-Rabbit IgG (H+L) Highly Cross-Adsorbed Secondary Antibody, Alexa Fluor 680 (Invitrogen #A10043).

Mouse immunohistochemistry: All tissue processing, staining, and analysis was blinded and scored in duplicate. Immunohistochemical staining was performed on 4-micron thick sections of formalin-fixed, paraffin-embedded tissues. Sections were air-dried and then melted in a 60°C oven for 30 minutes. Slides were loaded onto the Ventana Discovery automated staining instrument (Ventana Medical Systems, Tucson, AZ), de-paraffinized with the EZ Prep solution. Antigen retrieval was performed with CC1 (Cell Conditioning 1, pH 8.5) for 32–60 minutes at 95°C depending on the primary antibody. For host mo use

antibodies, mouse Detective (mouse protein blocker, BioCare Medical) is applied for 40 minutes at 35 degrees C. Primary antibody incubations (β-catenin: BD Biosciences cat. 610153, Cleaved-Caspase-3: Cell Signaling #9664, Ki-67: ab15580) was applied for 1 hour at 35–37°C — dilutions specified in the KEY Resources Table. A secondary antibody reagent (goat anti-rabbit: Sigma cat. #B8895, rabbit anti-mouse F(ab')2: Dako cat. #E0413) was applied for 24–60 minutes at 37°C. Positive signal was visualized using the DAB Map detection kit, which is a goat anti-mouse/anti-rabbit secondary HRP biotinylated detection system, utilizing DAB (3–3' diaminobenzidine) as the chromogen. Tissue sections were counterstained with hematoxylin for 12 minutes. The slides were removed from the immunostainer and placed in a dH2O/DAWN ™ mixture. The sections were gently washed in a mixture of de-ionized water and DAWN™ solution to remove any coverslip oil applied by the automated instrument. The slides were gently rinsed in deionized water until all of wash mixture was removed. The slides were de-hydrated in graded ethanols, cleared in xylene and then coverslipped.

Slides were scanned with the Zeiss AxioScan Z1 at the Fluorescence Microscopy Core Facility, a part of the Health Sciences Cores at the University of Utah for 20X images and measurements made using ZEN 2 and ZEN lite software. Microscopy equipment was obtained using a NCRR Shared Equipment Grant # 1S10RR024761–01. 4X, 10X, 20X and 40X representative images were obtained on an Olympus IX71 microscope, using MicroSuite software. Images were processed in Adobe Photoshop, with exposure times and adjustments identical between genotypes and tumor model groups.

Pathologic grading and quantification of proliferation.—Histological grading was performed by a board-certified pathologist with subspecialty training in gastrointestinal pathology (KJE) on representative H&E-stained (H&E) slides from the two models of carcinogenesis, AOM-DSS and *Apc* LOH, at the following respective time points: days 49 and 100 (all mice) and days 90 (all mice) and 140 ($Apc^{VillKO/+}$ only). H&E slides were blinded as to time-point, experiment, and genotype, and each tumor was assessed for size and grade. Photographs of slides, stained for Ki67 as described above, were taken of distal colon adenomas in the area of highest labelling by KJE. Printouts of photographs were blinded for quantification of proliferation by Ki67+ nuclei. Five researchers performed counts for both positive and negative nuclei in adenoma tissue from two tumor models and both *Mpc1*-deleted and control mice, excluding non-epithelial nuclei. Results were tabulated by image, then unblinded for comparison. All specimens generated were included in analysis. No subjects or data was excluded from analysis.

***Drosophila* MARCM clonal analysis:** The MARCM system was used to generate GFP-marked clones in the adult intestine, as described (Wu and Luo, 2006). Four to five day old adult female flies of the following genotypes were subjected to one 38°C heat pulse for 60 minutes to generate GFP-marked clones in the intestine. **Control:** *y, w, hs-FLP, UAS-GFP / w ; +; Tub-GAL4, FRT82B, Tub-Gal80 / FRT82B;* ***dMpc1* mutant:** *y, w, hs-FLP, UAS-GFP / w; +; Tub-GAL4, FRT82B, Tub-Gal80 / FRT82B dMpc1*^{1}; ***dMpc1 RNAi*:** *y, w, hs-FLP, UAS-GFP / w; + / UAS-dMpc1 RNAi; Tub-GAL4, FRT82B, Tub-Gal80 / FRT82B*; ***dMpc1/2* overexpression:** *y, w, hs-FLP, UAS-GFP / w; + / UAS-dMpc1-dMpc2; Tub-*

GAL4, FRT82B, Tub-Gal80 / FRT82B; **LDH RNAi:** *y, w, hs-FLP, UAS-GFP / w; + / UAS-LDH RNAi; Tub-GAL4, FRT82B, Tub-Gal80 / FRT82B;* **Apc1 Apc2 mutant:** *y, w, hs-FLP, UAS-GFP / w; +; Tub-GAL4, FRT82B, Tub-Gal80 / FRT82B* $Apc1^{Q8}$ $Apc2^{N175K}$ **Apc1 Apc2 mutant with *dMpc1 RNAi*:** *y, w, hs-FLP, UAS-GFP / w; + / UAS-Mpc1 RNAi; Tub-GAL4, FRT82B, Tub-Gal80 / FRT82B* $Apc1^{Q8}$ $Apc2^{N175K}$; **Apc1 Apc2 mutant with *dMpc1/2* overexpression:** *y, w, hs-FLP, UAS-GFP / w; + / UAS-dMPC-dMpc2 ; Tub-GAL4, FRT82B, Tub-Gal80 / FRT82B* $Apc1^{Q8}$ $Apc2^{N175K}$; **Apc1 Apc2 mutant with *LDH RNAi*:** *y, w, hs-FLP, UAS-GFP / w ; + / UAS-LDH RNAi ; Tub-GAL4, FRT82B, Tub-Gal80 / FRT82B* $Apc1^{Q8}Apc2^{N175K}$. Clones were analyzed at 5 days (most experiments) or 20 days (Figure 2F–J) after induction. The number of nuclei in GFP-expressing clones was used to quantify clone size. GFP was detected by fluorescence and nuclei were detected by DAPI stains.

For *Notch* RNAi studies, intestines were analyzed 7 days after clone induction. Animals of the following genotype were used: ***Notch*** **RNAi:** *y, w, hs-FLP, UAS-GFP / w ; UAS-Notch-RNAi; Tub-GAL4, FRT82B, Tub-GAL80 / FRT82B* ***Notch*** **RNAi with *dMpc1/2* overexpression:** *y, w, hs-FLP, UAS-GFP / w; UAS-Notch-RNAi/ UAS-dMpc1-dMpc2; Tub-GAL4, FRT82B, Tub-GAL80;* ***Notch*** **RNAi with *LDH*** **RNAi:** *y, w, hs-FLP, UAS-GFP / w; UAS-Notch-RNAi/ UAS-LDH RNAi; Tub-GAL4, FRT82B, Tub-GAL80.*

Drosophila **histology and immunostaining.—**Intestines were dissected in 1xPBS and fixed with 4% formaldehyde (Polysciences Inc, EM grade) overnight at 4°C. Tissues were washed four times with 0.1% Triton, 1xPBS (PBST) and incubated with mouse anti-Pros antibodies (DSHB) diluted 1:100 in PBST or 1:50 diluted rabbit antibodies directed against dMPC1 and dMPC2 at 4°C overnight (Colca et al., 2013). The ti ssues were then washed and incubated for 3–4 hours with either donkey anti-mouse Cy3-conjugated secondary antibodies (Jackson 715-165-157) or donkey anti-rabbit Cy3-conjugated secondary antibodies (Jackson 715– 165–152). Samples were mounted using Vectashield (Vector, USA) with DAPI. Images were acquired using an Olympus FV1000 confocal microscope and assembled into Z stack projections for the figures. Quantitation of the number of cells per clone is shown as a scatter plot with each data point representing the clone size in a single intestine.

Mouse intestinal crypt and tumor isotope labeling: _ For isotope labeling metabolomics, U-^{13}C-Palmitate, U-^{13}C -Glucose, and U-^{13}C -Glutamine labeling was performed in parallel on both normal crypts from control and $Mpc1^{Lrig1KO}$ mice and on tumors from $Apc^{Lrig1KO/+}$ and $Apc^{Lrig1KO/+}$ $Mpc1^{Lrig1KO}$ were sacrificed 30 or 90 days following tamoxifen administration, respectively. Crypts were isolated and tumors dissected as described above. Normal crypts were counted, and 10,000 crypts were seeded per well of a 6 well plate coated in a 10% Matrigel/90%DMEM-base mixture. Crypts were overlaid with 2mL DMEM media containing growth factors (Wnt-3a, EGF, Noggin, R-spondin), 5 μM CHIR99021, 1 mM NAC, 1 μg/ml L-carnitine, and 150 M U-^{13}C - Palmitate (Cambridge, CLM-409) conjugated to fatty acid-free BSA, or 25 M U-^{13}C-Glucose (Cambridge, CLM-1396), or 5 M U-^{13}C-L-Glutamine (Cambridge, CLM-1822). In each heavy labeled media type, the other carbon sources in identical ^{12}C were added, with the

exception of the experiment to determine the effect of exogenous palmitate on glucose utilization. Crypts were incubated for 90 minutes and then spun down in ice cold labeling media to remove Matrigel and resuspended in 100ul of extraction buffer (40% methanol, 40% Acetonitrile, 20%water, all LC/MS grade with 0.5% formic acid). Samples were vortexed and placed on ice. Within five minutes, samples were neutralized by adding 15% ammonium bicarbonate (amount determined before each experiment), vortexed again and returned to ice for 10 minutes. Samples were cleared in a cold centrifuge at max speed for 10 minutes. For tumor tracing, 3–5 tumors were placed per well of a 6 well plate in 2mL DMEM media as described above. After 90 minutes, tumors were washed in warm saline (0.9M NaCl), weighed and snap-frozen in liquid nitrogen. For the tumor tissue extraction, each sample was transferred to 2.0ml ceramic bead mill tubes (bioExpress). To each sample was added cold 90% methanol (MeOH) solution to give a rough final concentration of 80% MeOH to each tissue sample. The samples were then homogenized in an OMNI Bead Ruptor 24. Homogenized samples were then incubated at −20°C for 1 hr. After incubation the samples were centrifuged at 20,000 × g for 10 minutes at 4°C. The supernatant was then transferred from each bead mill tube into a labeled, fresh micro centrifuge tubes. Pooled quality control samples were made by removing a fraction of collected supernatant from each sample. Process blanks were made using only extraction solvent and went through the same process steps as the real samples. All samples, crypt and tumor, were then dried *en vacuo*.

LC-MS tracing analysis for crypts & tumors: Extracted polar metabolite samples were analyzed by LC-MC. Separation was achieved by hydrophilic interaction liquid chromatography (HILIC) using a Vanquish HPLC system (ThermoFisher Scientific). The column was an Xbridge BEH amide column (2.1 mm × 150mm, 2.5 μM particular size, 130Å pore size, Waters Co.) run with a gradient of solvent A (20 mM ammonium hydroxide, 20 mM ammonium acetate in 95:5 acetonitrile:Water, pH 9.5) and solvent B (100% acetonitrile) at a constant flow rate of 150 uL/min. The gradient function was: 0 min, 90% B; 2 min, 90% B; 3 min, 75% B; 7 min, 75% B; 8 min, 70% B; 9 min, 70% B; 10 min, 50% B; 12 min, 50% B; 13 min, 25% B; 14 min, 25% B; 16 min, 0% B; 20.5 min, 0% B; 21 min; 90% B; 25 min, 90% B. Autosampler temperature was 4°C, column temperature 30°C and injection volume 2 μL. Samples were injected by electrospray ionization into a QExactive HF orbitrap mass spectrometer (ThermoFisher Scientific) operating in negative ion mode with a resolving power of 120,000 at m/z of 200 and a full scan range of 75–1000 m/z. Data were analyzed using the MAVEN software package and specific peaks assigned based on exact mass and comparison with known standards (Melamud et al., 2010). Extracted peak intensities were corrected for natural isotopic abundance using the R package AccuCor (Su et al., 2017). No subjects or data was excluded from analysis.

GC-MS analysis for crypts & tumors: All GC-MS analysis was performed with an Agilent 5977b GC-MS MSD-HES and an Agilent 7693A automatic liquid sampler. Dried samples were suspended in 40 μL of a 40 mg/mL O-methoxylamine hydrochloride (MOX) (MP Bio #155405) in dry pyridine (EMD Millipore #PX2012–7) and incubated for one hour at 37 °C in a sand bath. 25 μL of this solution was added to auto sampler vials. 60 μL of N-methyl-N- trimethylsilyltrifluoracetamide (MSTFA with 1%TMCS, Thermo #TS48913) was

added automatically via the auto sampler and incubated for 30 minutes at 37 °C. After incubation, samples were vortexed and 1 μL of the prepared sample was injected into the gas chromatograph inlet in the split mode with the inlet temperature held at 250°C. A 1:1 split ratio was used for this analysis. The gas chromatograph had an initial temperature of 60°C for one minute followed by a 10°C/min ramp to 325°C held fo r 5 min. Then a 100°C/min ramp to 375°C and a final hold time of 5 minutes. A 30-meter Zebron ZB-5HT with 5m inert guard capillary column was employed for chromatographic separation. Helium was used as the carrier gas at a rate of 1 mL/min. Peak picking was performed using Agilent MassHunter software and isotopically corrected using a custom version of AccuCor that incorporated silicon. No subjects or data was excluded from analysis.

Mouse tissue gene expression profiling.—Whole crypts samples were selected either as untreated normal crypts or as adjacent normal crypts selected at random with inclusion criteria as an adenoma from the same mouse included. Whole crypts were extracted for RNA using QIAGEN RNeasy kit. Two methods were used to obtain tumor tissue for molecular analysis. A subset of tumor tissue was micro-dissected from formalin-fixed paraffin embedded colon samples, and RNA was extracted using Qiagen FFPE RNeasy kit (cat: 73504). A second set of tumor tissue was dissected from the normal mucosa under an Olympus SZ61 dissecting microscope in ice cold PBS, then snap frozen in liquid nitrogen. RNA was extracted using the Qiagen RNeasy (cat: 74104). FFPE extracted RNA and frozen tissue RNA were comparable in quality and concentration, and used in parallel in subsequent studies. Gene expression was profiled by transcript abundance using the NanoString Elements platform according to the manufacturer's protocols. The custom 22 gene probe set, described previously, includes intestinal specific stem and differentiation markers, MPC1 and MPC2 (Schell et al. 2017). Using the NanoString nSolver 4 analysis software, raw counts were corrected by background thresholding with geometric mean factor normalization, and genes were mean centered for heatmap generation, and two adenomas from AOM-DSS experiments were excluded for raw and normalized gene expression with geometric means deviating 2-fold from the dataset average. Plots were generated for principle component analysis using XPRESSplot (Berg 2019 bioRxiv). Gene normalizations were performed with scikit-learn (v0.21.3) (Buitinck et al. 2013), and other statistical measures were calculated using SciPy (v1.3.0) (Jones et al. 2019) and StatsModels (v0.10.1) (Seabold et al. 2010) within the Python (v3.7.3) environment. A perpetually-available archive of the data and code used for pertinent analyses and figures not generated by Prism GraphPad (v7) is available at https://doi.org/10.5281/zenodo.3377989 (Berg 2019).

Human Datasets for normal mucosa, adenomas, adenocarcinoma: Human data was accessed from the GEO database (GSE20916 and GSE8671) under inclusion parameters of normal tissue and non-cancer adenoma tissue. Unified GTEx and TCGA data for colon cancer (COAD) were obtained from (Wang et al. 2018). For microarray datasets, multimapping probes were dropped and probe sets mapping to the same gene were collapsed. For the GTEx/TCGA data, expression levels were mean-centered (z-score) and any z-score > 5 for the analyzed gene set was thresholded at 5 to prevent high signal from concealing expression data falling within a more "normal" range. This can be explored more in the interactive notebook (Berg 2019). Plots were generated and principle component

analysis were performed using XPRESSplot (Berg 2019 bioRxiv). Gene normalizations were performed with scikit-learn (v0.21.3) (Buitinck et al. 2013), and other statistical measures were calculated using SciPy (v1.3.0) (Jones et al. 2019) and StatsModels (v0.10.1) (Seabold et al. 2010) within the Python (v3.7.3) environment. A perpetually-available archive of the data and code used for pertinent analyses and figure generation not generated by Prism GraphPad (v7) is available at https://doi.org/10.5281/zenodo.3377989 (Berg 2019).

The custom pyruvate metabolic gene set was composed of the KEGG pyruvate metabolism annotation with select genes included from KEGG Glycolysis/Gluconeogenesis, KEGG TCA cycle, KEGG Monocarboxylate transporters, and glucose transporters. This list thus includes relevant enzymes and transporters, core and offshoot pathways of pyruvate metabolism to better address whether the pyruvate metabolic gene program shifts during tumor initiation. A complete gene list as well as the origin lists are available at https://doi.org/10.5281/zenodo.3377989 (Berg 2019).

A linear least-squares regression was used to calculate correlation coefficients for *Mpc1* or *Mpc2* against every gene and r >/= 0.60 (p-value < 0.01) was used as a cut-off. Correlated and anti-correlated gene lists were analyzed by DAVID (v6.8) and PANTHER (v13.1) to determine enriched pathways within these gene cohorts. $-\log_{10}$(p-values) were reported. All code necessary to reproduce the Figures and select tables can be found at https://doi.org/10.5281/zenodo.3377989 (Berg 2019). Resulting pathway lists were parsed for pathways relevant to stem cell maintenance, growth signaling, cancer pathways, and colon-specific pathways, with a p-value <0.05. Correlation Gene Lists with *Mpc1* and *Mpc2*, and table summaries from DAVID and PANTHER are available at https://doi.org/10.5281/zenodo.3377989 (Berg 2019).

QUANTIFICATION AND STATISTICAL ANALYSIS

Prior to rodent studies and in accordance with IACUC protocols, we performed a power analysis for both the AOM-DSS and *Apc* loss of heterozygosity mouse experiments to determine cohort sizes of 30 and 10, respectively including both male and female mice. All mouse studies were performed in smaller rolling cohorts of 5–7 mice per time-point and no cohort to cohort variation could account for the phenotypes observed. All assays and studies, excluding the NanoString gene expression assay, were performed with technical replicates (n=3) or with multiple blinded researchers where appropriate. In the NanoString gene expression assays, a minimum of biological replicates (n=3) were examined. All statistics and significance unless otherwise stated were performed in Prism GraphPad (v6–7), using unpaired student t-test's, Chi-square tests, and one-way ANOVA with multiple comparisons with Sidak multiple test correction where appropriate. Other analysis archived at https://doi.org/10.5281/zenodo.3377989 used an FDR-corrected Wilcoxon rank-sums test for statistical significance. The lines and error bars depict the average ± the standard deviation (Berg 2019).

DATA AND CODE AVAILABILITY

The code and data are available at https://doi.org/10.5281/zenodo.3377989 (Berg 2019). This study did not generate the human data, which was accessed from the GEO database

(GSE20916 and GSE8671) and unified GTEx and TCGA data for colon cancer (COAD) were obtained from (Wang et al. 2018). The Nanostring mouse adenoma and crypt data generated by this study are available on the GEO database (GSE136710).

Supplementary Material

Refer to Web version on PubMed Central for supplementary material.

Acknowledgments

We thank O. Yilmaz for mouse strains, M. Disotaur and B. Lamar Smith for assistance in adenoma proliferation counts, J. O'Shea and N. Bronson for Nanostring analysis, S. Tripp for histological and staining assistance, K. Goryca and J. Ostrowski for help with analysis of human tissue samples, C. Micchelli and B. Edgar for providing fly stocks, G. Lam for *Drosophila* technical support, J. Gertz, K. Beebe and J. Tennessen for helpful discussions, the Bloomington Stock Center for fly stocks (NIH P40OD018537), and FlyBase for informatic support. We thank J. Cox and T. Van Ry for Metabolomics analysis performed at the Metabolomics Core Facility at the University of Utah which is supported by 1 S10 OD016232-01, 1 S10 OD021505-01 and 1S10OD018210-01A1. We thank S. Tripp and K. Barker for immunohistochemical expertise and support.

Funding

R01CA228346 to JR and CST and Nora Eccles Treadwell Foundation to JR; 1F30CA225110-01 to CB (2018-current), 4T32HD007491-21 to CB (2016-2018); 4R00CA215307-03 to GSD; 1T32DK11096601 to JAB (2018-current); JR is an Investigator of the Howard Hughes Medical Institute.

References

Bader DA, Hartig SM, Putluri V, Foley C, Hamilton MP, Smith EA, Saha PK, Panigrahi A, Walker C, Zong L, et al. (2019). Mitochondrial pyruvate import is a metabolic vulnerability in androgen receptor-driven prostate cancer. Nat Metab 1, 70–85. [PubMed: 31198906]

Barker N, Ridgway RA, van Es JH, van de Wetering M, Begthel H, van den Born M, Danenberg E, Clarke AR, Sansom OJ, and Clevers H (2009). Crypt stem cells as the cells-of-origin of intestinal cancer. Nature 457, 608–611. [PubMed: 19092804]

Berg JA. (2019). j-berg/bensard_figures_2019: Manuscript Resubmission (update) (Version v0.0.2). Zenodo. 10.5281/zenodo.3379036

Berg JA, Belyeu JR, Morgan JT, Bott AJ, Ouyang Y, Quinlan AR, Gertz J, Rutter J (2019). XPRESSyourself: Enhancing and Automating the Ribosome Profiling and RNA-Seq Analysis Toolkit. bioRxiv 704320; doi: 10.1101/704320

Beyaz S, Mana MD, Roper J, Kedrin D, Saadatpour A, Hong S-J, Bauer-Rowe KE, Xifaras ME, Akkad A, Arias E, et al. (2016). High-fat diet enhances stemness and tumorigenicity of intestinal progenitors. Nature 531, 53–58. [PubMed: 26935695]

Bricker DK, Taylor EB, Schell JC, Orsak T, Boutron A, Chen YC, Cox JE, Cardon CM, Van Vranken JG, Dephoure N, et al. (2012). A Mitochondrial Pyruvate Carrier Required for Pyruvate Uptake in Yeast, Drosophila, and Humans. Science 337, 96–100. [PubMed: 22628558]

Buescher JM, et al. (2015). A roadmap for interpreting 13C metabolite labeling patterns from cells. Current Opinion in Biotechnology, 34 (2015) 189–201. [PubMed: 25731751]

Buitinck L, Louppe G, Blondel M, Pedregosa F, Mueller A, Grisel O, Niculae V, Prettenhofer P, Gramfort A, Grobler J, Layton R, VanderPlas J, Joly A,Holt B, Varoquaux G (2013). API design for machine learning software: experiences from the scikitlearnn project. ECML PKDD Workshop: Languages for Data Mining and Machine Learning, pp. 108–122.

Charlton-Perkins MA, Sendler ED, Buschbeck EK, and Cook TA (2017). Multifunctional glial support by Semper cells in the Drosophila retina. PLoS Genet 13, e1006782. [PubMed: 28562601]

Cheng CW, Biton M, Haber AL, Gunduz N, Eng G, Gaynore LT, Tripathi S, Calibasi-Kocal G, Rickelt S, Butty VL, Morena-Serrano M, et al. (2019). Ketone Body Signaling Mediates Intestinal Stem Cell Homoestasis and Adaption to Diet. Cell 178, 1115–1131. [PubMed: 31442404]

Colca JR, McDonald WG, Cavey GS, Cole SL, Holewa DD, Brightwell-Conrad AS, Wolfe CL, Wheeler JS, Coulter KR, Kilkuskie PM, et al. (2013). Identification of a mitochondrial target of thiazolidinedione insulin sensitizers (mTOT)--relationship to newly identified mitochondrial pyruvate carrier proteins. PLoS One 8, e61551. [PubMed: 23690925]

Colnot S, Niwa-Kawakita M, Hamard G, Godard C, Le Plenier S, Houbron C, Romagnolo B, Berrebi D, Giovannini M, and Perret C (2004). Colorectal cancers in a new mouse model of familial adenomatous polyposis: influence of genetic and environmental modifiers. Laboratory Investigation 84, 1619–1630. [PubMed: 15502862]

Cordero JB, Stefanatos RK, Myant K, Vidal M, and Sansom OJ (2012). Non-autonomous crosstalk between the Jak/Stat and Egfr pathways mediates Apc1-driven intestinal stem cell hyperplasia in the Drosophila adult midgut. Development 139, 4524–4535. [PubMed: 23172913]

Dow LE, O'Rourke KP, Simon J, Tschaharganeh DF, van Es JH, Clevers H, and Lowe SW (2015). Apc Restoration Promotes Cellular Differentiation and Reestablishes Crypt Homeostasis in Colorectal Cancer. Cell 161, 1539–1552. [PubMed: 26091037]

Emig D, Salomonis N, Baumbach J, Lengauer T, Conklin BR, Albrecht M (2010). AltAnalyze and DomainGraph: analyzing and visualizing exon expression data. Nucleic Acids Res. 38 Suppl:W755–62. [PubMed: 20513647]

Fantin VR, St-Pierre J, and Leder P (2006). Attenuation of LDH-A expression uncovers a link between glycolysis, mitochondrial physiology, and tumor maintenance. Cancer Cell 9, 425–434. [PubMed: 16766262]

Flores A, Schell J, Krall AS, Jelinek D, Miranda M, Grigorian M, Braas D, White AC, Zhou JL, Graham NA, et al. (2017). Lactate dehydrogenase activity drives hair follicle stem cell activation. Nat Cell Biol 19, 1017–1026. [PubMed: 28812580]

Goetzman ES, and Prochownik EV (2018). The Role for Myc in Coordinating Glycolysis, Oxidative Phosphorylation, Glutaminolysis, and Fatty Acid Metabolism in Normal and Neoplastic Tissues. Front Endocrinol (Lausanne) 9, 129. [PubMed: 29706933]

Gray LR, Sultana MR, Rauckhorst AJ, Oonthonpan L, Tompkins SC, Sharma A, Fu X, Miao R, Pewa AD, Brown KS, et al. (2015). Hepatic Mitochondrial Pyruvate Carrier 1 Is Required for Efficient Regulation of Gluconeogenesis and Whole-Body Glucose Homeostasis. Cell metabolism 22, 669–681. [PubMed: 26344103]

Grenell A, Wang Y, Yam M, Swarup A, Dilan TL, Hauer A, Linton JD, Philp NJ, Gregor E, Zhu S, et al. (2019). Loss of MPC1 reprograms retinal metabolism to impair visual function. Proc Natl Acad Sci U S A 116, 3530–3535. [PubMed: 30808746]

Hanahan D, and Weinberg RA (2011). Hallmarks of cancer: the next generation. Cell 144, 646–674. [PubMed: 21376230]

Herzig S, Raemy E, Montessuit S, Veuthey J-L, Zamboni N, Westermann B, Kunji ERS, and Martinou J-C (2012). Identification and Functional Expression of the Mitochondrial Pyruvate Carrier. Science 337, 93–96. [PubMed: 22628554]

Hong CS, Graham NA, Gu W, Espindola Camacho C, Mah V, Maresh EL, Alavi M, Bagryanova L, Krotee PAL, Gardner BK, et al. (2016). MCT1 Modulates Cancer Cell Pyruvate Export and Growth of Tumors that Co-express MCT1 and MCT4. Cell reports 14, 1590–1601. [PubMed: 26876179]

Huang DW, Sherman BT, and Lempicki RA (2009a). Bioinformatics enrichment tools: paths toward the comprehensive functional analysis of large gene lists. Nucleic Acids Research 37, 1–13. [PubMed: 19033363]

Huang DW, Sherman BT, and Lempicki RA (2009b). Systematic and integrative analysis of large gene lists using DAVID bioinformatics resources. Nature Protocols 4, 44–57. [PubMed: 19131956]

Hue L, and Taegtmeyer H (2009). The Randle cycle revisited: a new head for an old hat. Am J Physiol Endocrinol Metab 297, E578–591. [PubMed: 19531645]

Johnson RL, and Fleet JC (2012). Animal models of colorectal cancer. Cancer and Metastasis Reviews 32, 39–61.

Jones E, Oliphant E, Peterson P,et al.(2019). SciPy: Open Source Scientific Tools for Python. http://www.scipy.org/[Online; accessed 2019-08-27].

Lee WC, Beebe K, Sudmeier L, and Micchelli CA (2009). Adenomatous polyposis coli regulates Drosophila intestinal stem cell proliferation. Development 136, 2255–2264. [PubMed: 19502486]

Li H, Chawla G, Hurlburt AJ, Sterrett MC, Zaslaver O, Cox J, Karty JA, Rosebrock AP, Caudy AA, and Tennessen JM (2017). Drosophila larvae synthesize the putative oncometabolite L-2-hydroxyglutarate during normal developmental growth. Proc Natl Acad Sci U S A 114, 1353–1358. [PubMed: 28115720]

Marley AR, and Nan H (2016). Epidemiology of colorectal cancer. Int J Mol Epidemiol Genet 7, 105–114. [PubMed: 27766137]

Marjou El, F., Janssen KP, Chang BHJ, Li M, Hindie V, Chan L, Louvard D, Chambon P, Metzger D, Robine S (2004). Tissue-specific and inducible Cre-mediated recombination in the gut epithelium. genesis 39, 186–193. [PubMed: 15282745]

Melamud E, Vastag L, Rabinowitz JD (2010). Metabolomic analysis and visualization engine for LC-MS data. Anal. Chem 82, 9818–9826 [PubMed: 21049934]

Merlos-Suárez A, Barriga FM, Jung P, Iglesias M, Céspedes MV, Rossell D, Sevillano M, Hernando-Momblona X, da Silva-Diz V, Muñoz P, et al. (2011). The Intestinal Stem Cell Signature Identifies Colorectal Cancer Stem Cells and Predicts Disease Relapse. Stem Cell 8, 511–524.

Micchelli CA, and Perrimon N (2006). Evidence that stem cells reside in the adult Drosophila midgut epithelium. Nature 439, 475–479. [PubMed: 16340959]

Mihaylova MM, Cheng CW, Cao AQ, Tripathi S, Mana MD, Bauer-Rowe KE, Abu-Remaileh M, Clavain L, Erdemir A, Lewis CA, et al. (2018). Fasting Activates Fatty Acid Oxidation to Enhance Intestintal Stem Cell Function during Homeostasis and Aging. Cell Stem Cell 22, 769–778. [PubMed: 29727683]

Nusse R, and Clevers H (2017). Wnt/β-Catenin Signaling, Disease, and Emerging Therapeutic Modalities. Cell 169, 985–999. [PubMed: 28575679]

Ohlstein B, and Spradling A (2006). The adult Drosophila posterior midgut is maintained by pluripotent stem cells. Nature 439, 470–474. [PubMed: 16340960]

Ohlstein B, and Spradling A (2007). Multipotent Drosophila intestinal stem cells specify daughter cell fates by differential notch signaling. Science 315, 988–992. [PubMed: 17303754]

Olson KA, Schell JC, and Rutter J (2016). Pyruvate and Metabolic Flexibility: Illuminating a Path Toward Selective Cancer Therapies. Trends Biochem Sci 41, 219–230. [PubMed: 26873641]

Olsson A, Venkatasubramanian M, Chaudhri VK, Aronow BJ, Salomonis N, Singh H, Grimes HL (2016). Single-cell analysis of mixed-lineage states leading to a binary cell fate choice. Nature 537 (7622):698–702. [PubMed: 27580035]

Pavlova NN, and Thompson CB (2016). The Emerging Hallmarks of Cancer Metabolism. Cell metabolism 23, 27–47. [PubMed: 26771115]

Powell AE, Vlacich G, Zhao ZY, McKinley ET, Washington MK, Manning HC, and Coffey RJ (2014). Inducible loss of one Apc allele in Lrig1-expressing progenitor cells results in multiple distal colonic tumors with features of familial adenomatous polyposis. Am J Physiol Gastrointest Liver Physiol 307, G16–23. [PubMed: 24833705]

Powell AE, Wang Y, Li Y, Poulin EJ, Means AL, Washington MK, Higginbotham JN, Juchheim A, Prasad N, Levy SE, et al. (2012). The Pan-ErbB Negative Regulator Lrig1 Is an Intestinal Stem Cell Marker that Functions as a Tumor Suppressor. Cell 149, 146–158. [PubMed: 22464327]

Rauckhorst AJ, Gray LR, Sheldon RD, Fu X, Pewa AD, Feddersen CR, Dupuy AJ, Gibson-Corley KN, Cox JE, Burgess SC, et al. (2017). The mitochondrial pyruvate carrier mediates high fat diet-induced increases in hepatic TCA cycle capacity. Mol Metab 6, 1468–1479. [PubMed: 29107293]

Rauckhorst AJ, and Taylor EB (2016). Mitochondrial pyruvate carrier function and cancer metabolism. Curr Opin Genet Dev 38, 102–109. [PubMed: 27269731]

Romero-Garcia S, Moreno-Altamirano MM, Prado-Garcia H, and Sanchez-Garcia FJ (2016). Lactate Contribution to the Tumor Microenvironment: Mechanisms, Effects on Immune Cells and Therapeutic Relevance. Front Immunol 7, 52. [PubMed: 26909082]

Rosenberg DW, Giardina C, and Tanaka T (2009). Mouse models for the study of colon carcinogenesis. Carcinogenesis 30, 183–196. [PubMed: 19037092]

Sabates-Bellver J, van der Flier LG, de Palo M, Cattaneo E, Maake C, Rehrauer H, Laczko E, Kurowski MA, Bujnicki JM, Menigatti M, et al. (2007). Transcriptome Profile of Human Colorectal Adenomas. Mol Cancer Res 5, 1263–1275. [PubMed: 18171984]

Salomonis N, Schlieve CR, Pereira L, Wahlquist C, Colas A, Zambon AC, Vranizan K, Spindler MJ, Pico AR, Cline MS, Clark TA, Williams A, Blume JE, Samal E, Mercola M, Merrill BJ, Conklin BR (2010). Alternative splicing regulates mouse embryonic stem cell pluripotency and differentiation. Proc Natl Acad Sci U S A. 107(23):10514–9. [PubMed: 20498046]

Samanta D, and Semenza GL (2018). Metabolic adaptation of cancer and immune cells mediated by hypoxia-inducible factors. Biochim Biophys Acta Rev Cancer 1870, 15–22. [PubMed: 30006019]

Sandoval IT, Delacruz RG, Miller BN, Hill S, Olson KA, Gabriel AE, Boyd K, Satterfield C, Remmen HV, Rutter J, et al. (2017). A metabolic switch controls intestinal differentiation downstream of Adenomatous polyposis coli (APC). Elife 6, e22706. [PubMed: 28397687]

Sansom OJ, Meniel VS, Muncan V, Phesse TJ, Wilkins JA, Reed KR, Vass JK, Athineos D, Clevers H, and Clarke AR (2007). Myc deletion rescues Apc deficiency in the small intestine. Nature 446, 676–679. [PubMed: 17377531]

Schell JC, Olson KA, Jiang L, Hawkins AJ, Van Vranken JG, Xie J, Egnatchik RA, Earl EG, DeBerardinis RJ, and Rutter J (2014). A Role for the Mitochondrial Pyruvate Carrier as a Repressor of the Warburg Effect and Colon Cancer Cell Growth. Molecular Cell 56, 400–413. [PubMed: 25458841]

Schell JC, and Rutter J (2013). The long and winding road to the mitochondrial pyruvate carrier. Cancer Metab 1, 6. [PubMed: 24280073]

Schell JC, Wisidagama DR, Bensard C, Zhao H, Wei P, Tanner J, Flores A, Mohlman J, Sorensen LK, Earl CS, et al. (2017). Control of intestinal stem cell function and proliferation by mitochondrial pyruvate metabolism. Nat Cell Biol 19, 1027–1036. [PubMed: 28812582]

Seabold S, and Perktold J (2010). Statsmodels: Econometric and statistical modeling with python. Proceedings of the 9th Python in Science Conference.

Sohaily Al, S., Biankin A, Leong R, Corish MK, Warusavitarne J (2012). Molecular pathways in colorectal cancer. Journ of Gastroenterology and Hepatology 27, 1423–1431.

Skrzypczak M, Goryca K, Rubel T, Paziewska A, Mikula M, Jarosz D, Pachlewski J, Oledzki J, and Ostrowsk J (2010). Modeling Oncogenic Signaling in Colon Tumors by Multidirectional Analyses of Microarray Data Directed for Maximization of Analytical Reliability. PloS one 5, e13091. [PubMed: 20957034]

Slaninova V, Krafcikova M, Perez-Gomez R, Steffal P, Trantirek L, Bray SJ, and Krejci A (2016). Notch stimulates growth by direct regulation of genes involved in the control of glycolysis and the tricarboxylic acid cycle. Open Biol 6, 150155. [PubMed: 26887408]

Su X, Lu W, Rabinowitz JD (2017). Metabolite Spectral Accuracy on Orbitraps. Anal. Chem 89, 5940–5948. [PubMed: 28471646]

Sullivan LB, Gui DY, Hosios AM, Bush LN, Freinkman E, and Vander Heiden MG (2015). Supporting Aspartate Biosynthesis Is an Essential Function of Respiration in Proliferating Cells. Cell 162, 552–563. [PubMed: 26232225]

Sun S, Li H, Chen J, and Qian Q (2017). Lactic Acid: No Longer an Inert and End-Product of Glycolysis. Physiology (Bethesda) 32, 453–463. [PubMed: 29021365]

Thomas PD, Campbell MJ, Kejariwal A, Mi H, Karlak B, Daverman R, Diemer K, Muruganujan A, and Narechania A (2003). PANTHER: a library of protein families and subfamilies indexed by function. Genome Research 13, 2129–2141. [PubMed: 12952881]

Thomas PD, Kejariwal A, Guo N, Mi H, Campbell MJ, Muruganujan A, and Lazareva-Ulitsky B (2006). Applications for protein sequence–function evolution data: mRNA/protein expression analysis and coding SNP scoring tools. Nucleic Acids Research 34, W645–W650. [PubMed: 16912992]

Tomasetti C, Li L, and Vogelstein B (2017). Stem cell divisions, somatic mutations, cancer etiology, and cancer prevention. Science 355, 1330–1334. [PubMed: 28336671]

van der Flier LG, and Clevers H (2009). Stem cells, self-renewal, and differentiation in the intestinal epithelium. Annu Rev Physiol 71, 241–260. [PubMed: 18808327]

Vander Heiden MG, Cantley LC, and Thompson CB (2009). Understanding the Warburg Effect: The Metabolic Requirements of Cell Proliferation. Science 324, 1029–1033. [PubMed: 19460998]

Vander Heiden MG, and DeBerardinis RJ (2017). Understanding the Intersections between Metabolism and Cancer Biology. Cell 168, 657–669. [PubMed: 28187287]

Vogelstein B, Fearon ER, Hamilton SR, Kern SE, Preisinger AC, Leppert M, Smits AMM, and Bos JL (2010). Genetic Alterations during Colorectal-Tumor Development. N Engl J Med 319, 525–532.

Vogelstein B, and Kinzler KW (2015). The Path to Cancer --Three Strikes and You're Out. N Engl J Med 373, 1895–1898. [PubMed: 26559569]

Wang Q, Armenia J, Zhang C, et al. (2018). Unifying cancer and normal RNA sequencing data from different sources. Sci Data. 5, 180061. doi:10.1038/sdata.2018.61 [PubMed: 29664468]

Weinberg BA, and Marshall JL (2019). Colon Cancer in Young Adults: Trends and Their Implications. Curr Oncol Rep 21, 3. [PubMed: 30659375]

Wu JS, and Luo L (2006). A protocol for mosaic analysis with a repressible cell marker (MARCM) in Drosophila. Nat Protoc 1, 2583–2589. [PubMed: 17406512]

Xie H, Hanai J, Ren JG, Kats L, Burgess K, Bhargava P, Signoretti S, Billiard J, Duffy KJ, Grant A, et al. (2014). Targeting lactate dehydrogenase--a inhibits tumorigenesis and tumor progression in mouse models of lung cancer and impacts tumor-initiating cells. Cell metabolism 19, 795–809. [PubMed: 24726384]

Xie H, and Simon MC (2017). Oxygen availability and metabolic reprogramming in cancer. J Biol Chem 292, 16825–16832. [PubMed: 28842498]

Yang C, Ko B, Hensley CT, Jiang L, Wasti AT, Kim J, Sudderth J, Calvaruso MA, Lumata L, Mitsche M, et al. (2014). Glutamine Oxidation Maintains the TCA Cycle and Cell Survival during Impaired Mitochondrial Pyruvate Transport. Molecular Cell 56, 414–424. [PubMed: 25458842]

Highlights

- Intestinal tumors exhibit low Mitochondrial Pyruvate Carrier (MPC) expression
- MPC inactivation is sufficient to promote intestinal tumor formation in mice and flies.
- MPC overexpression in the fly is sufficient to prevent oncogene-induced tumorigenesis.
- MPC expression correlates negatively with expression of Wnt/β-catenin target genes.

Context and Significance

The scientific community has clearly demonstrated in recent years that cancer cells exhibit atypical metabolic characteristics and can, in many cases, become dependent on those features. Here, researchers at the University of Utah aimed to determine whether cancer initiation also involves a change in cellular metabolic state. Indeed, the authors found that enforcing a more “tumorigenic” metabolic behavior led to an increased incidence of tumors in both mouse and fly models. Moreover, they found that prevention of this “tumorigenic” metabolic profile can block cancerous growth in response to otherwise strongly tumorigenic stimulation. These results demonstrate that the cellular metabolic program is necessary and sufficient to impact the incidence of tumor formation and lays the foundation for future work to determine how changes in this program can decrease human tumor formation.

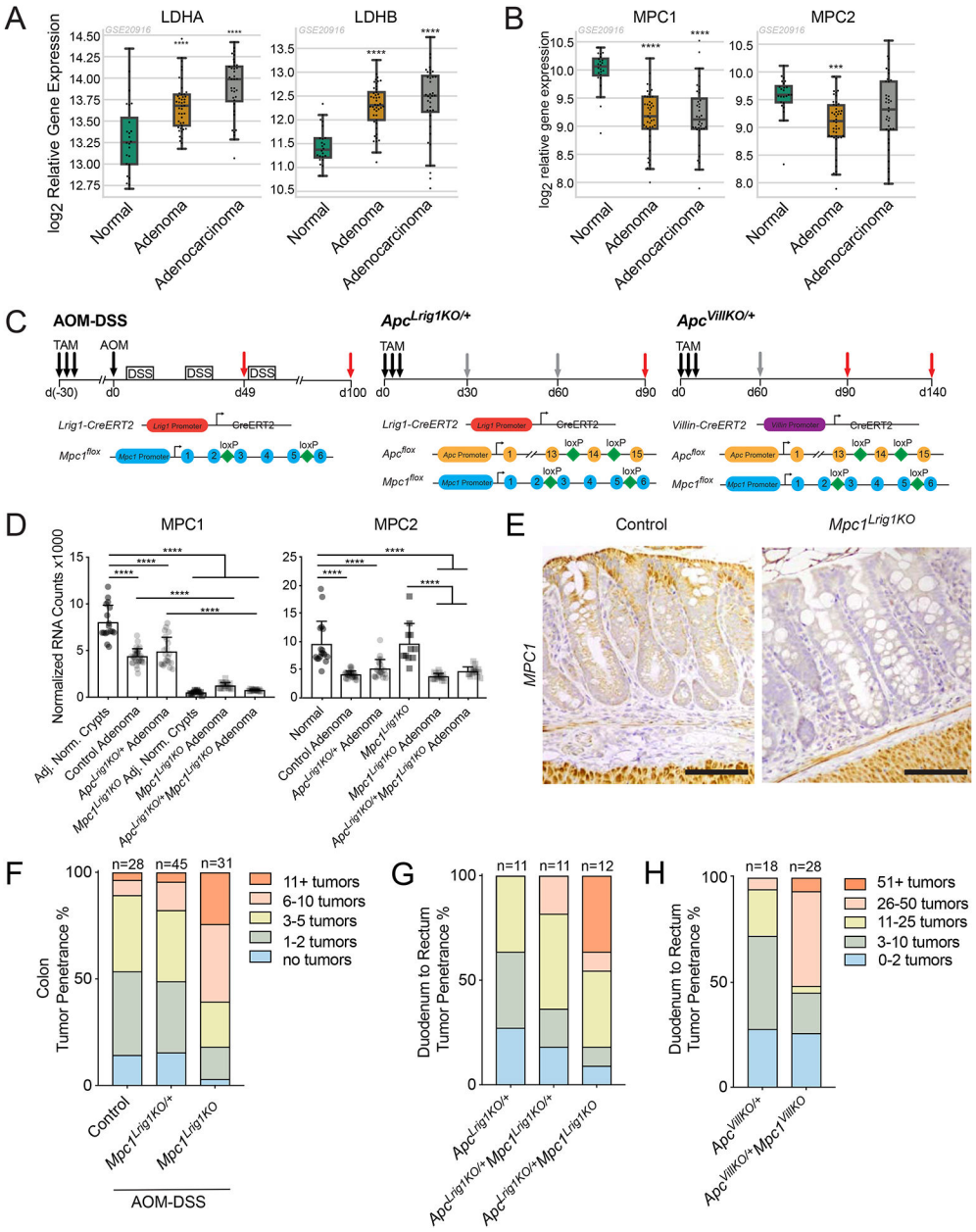

Figure 1: Decreased MPC expression is a feature of and predisposes for tumor initiation.

(A-B) Normalized $\log_2$ expression levels of *LDHA*, *LDHB* (A), *Mpc1* and *Mpc2* (B) mRNA relative abundance in human colon normal tissue (green), adenomas (orange), and adenocarcinomas (grey) from dataset GSE20916 (n=24–45 per group), ****FDR≤0.0001;***FDR≤0.001, FDR-corrected Wilcoxon rank-sums test, error bars SD. See also Figure S1A–D, Berg 2019. (C) 8 to 12 week-old transgenic mice were injected intraperitoneally three consecutive days with tamoxifen (TAM;20mg/day), then 30 days later, injected with azoxymethane (AOM; 10mg/mL/kg body weight). One week post-AOM, mice began three cycles of five days on 2% dextran sodium sulfate (DSS) in the drinking water, sixteen days on fresh drinking water. Tumor burden was assessed at 49 and 100 days post-AOM (red arrows). Schematics of the *Mpc1*^{flox} and *Lrig1-CreERT2* alleles are shown.

8 to 12 week-old transgenic mice were injected intraperitoneally three consecutive days with tamoxifen (TAM; 20mg/day), then examined at 30, 60, or 90 days post-TAM (red arrows). Schematics of the *Mpc1*^{flox}, *Apc*^{flox}, and *Lrig1-CreERT2* alleles are shown. 8 to 12 week-old transgenic mice were injected intraperitoneally three consecutive days with tamoxifen (TAM; 20mg/day), then examined at 60, 90, or 140 days post-TAM (red arrows). Schematics of the *Mpc1*^{flox}, *Apc*^{flox}, and *Villin-CreERT2* alleles are shown. 8 to 12 week-old transgenic mice were injected intraperitoneally three consecutive days with tamoxifen (TAM; 20μg/day), then examined at 60, 90, or 140 days post-TAM (red arrows). (D) Normalized RNA counts for *Mpc1* (left) and *Mpc2* (right) of isolated adjacent normal colon crypts and adenomas from the two main tumor models, both control and *Apc*$^{Lrig1KO/+}$ crypts and adenomas, then *Mpc1*^{Lrig1lKO} and *Apc*$^{Lrig1KO/+}$*Mpc1*^{Lrig1KO} crypts and adenomas (normal crypts n=10–17, adenomas n=16–32), ****p≤0.0001, one-way ANOVA with multiple comparisons, error bars SD. (E) Anti-MPC1 staining of colon sections at 60 days post-TAM (40X, scale bars = 100μm). (F) At 100 days post-AOM, tumor burden (bins of lesion number per mouse) were assessed in *Mpc1*^{Lrig1KO} and control mice (n=28–45 mice). (G) At 90 days post-TAM tumor burden (bins of lesion number per mouse) were assessed in *Apc*$^{Lrig1KO/+}$*Mpc1*^{Lrig1KO} and *Apc*$^{Lrig1KO/+}$ mice (n=11–12). (H) At 140 days post-TAM, tumor penetrance (having one or more lesions per mouse) and burden (bins of lesion number per mouse) were assessed in *Apc*$^{VillKO/+}$*Mpc1*^{VillKO} and *Apc*$^{VillKO/+}$mice (n=18–28).

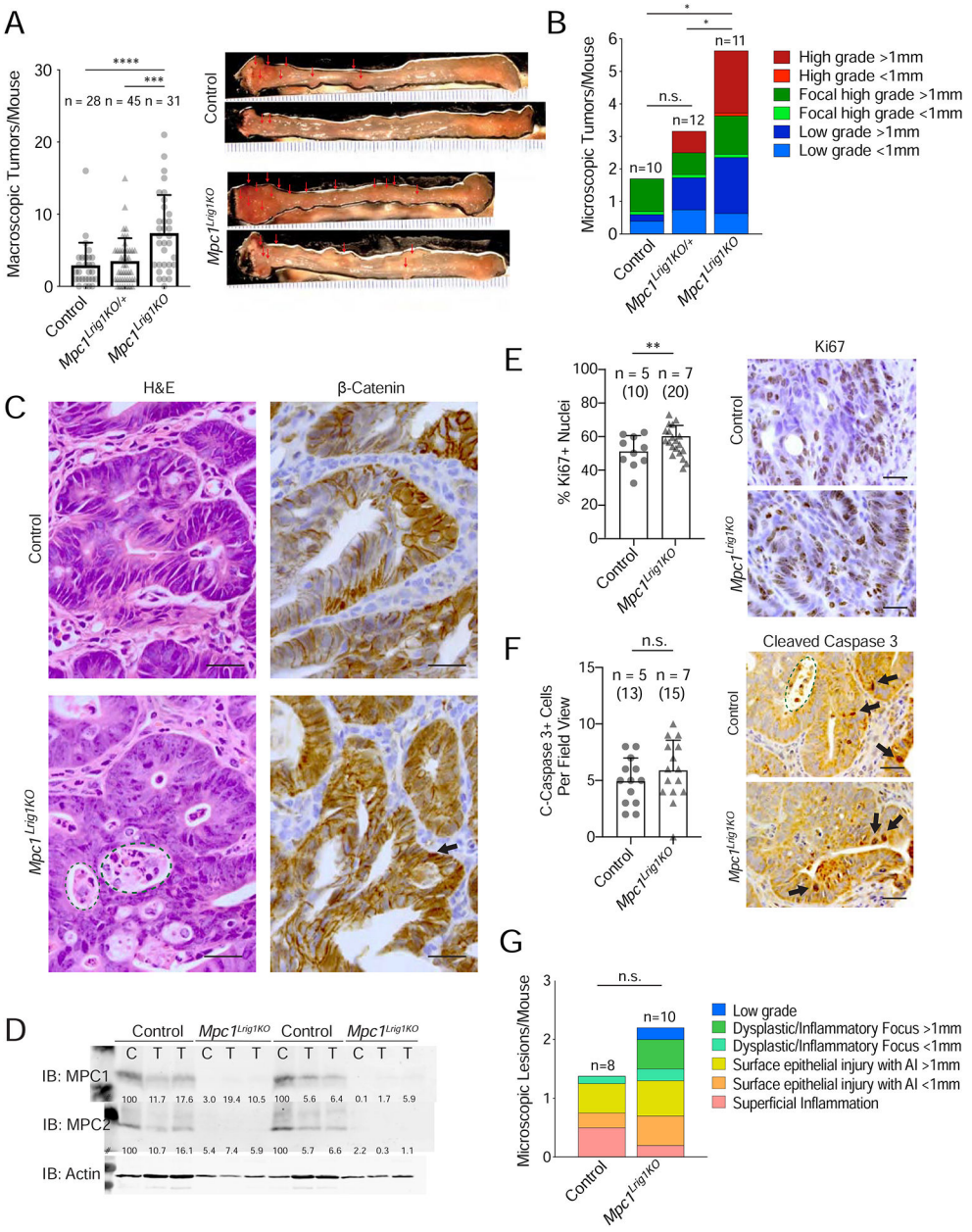

Figure 2: Loss of *Mpc1* accelerates tumor initiation and dysplastic progression in the environmental tumor model.

(A) Macroscopic tumor burden was assessed in *Mpc1*^{Lrig1KO}, *Mpc1*$^{Lrig1KO/+}$, and control mice at 100 days post-AOM (n=28–45 mice), ****p≤0.0001, ***p≤0.001, one-way ANOVA with multiple comparisons. Representative gross colon tumor burden and distribution are shown (ruler tick = 1mm). (B) At 100 days post-AOM, microscopic tumor grade and size assessed by pathologic grading in colons of *Mpc1*^{Lrig1KO}, *Mpc1*$^{Lrig1KO/+}$, and control mice (n=10–12), n.s.=not significant, *p≤0.05, one-way ANOVA with multiple comparisons on number of microscopic tumors per mouse. (C) Hematoxylin/Eosin and anti-β-catenin staining of control and *Mpc1*^{Lrig1KO} adenomas at 100 days post-AOM, (100X, scale bars = 25μm). Black arrows indicate nuclear β-catenin. Green dashed circles indicate crypt

necrosis. (D) Immunoblot of paired normal crypts (“C”) and tumor (“T”) samples from two control mice and two *Mpc1*^{Lrig1KO} mice for MPC1, MPC2, and actin. Densitometry for MPC1 and MPC2, normalized to actin is shown with relative values adjusted to 100 for each control mouse normal crypt sample. (E) 100 days post-AOM, Ki67-positive nuclei as a percentage of total adenoma nuclei of *Mpc1*^{Lrig1KO} and control adenomas were quantified on blinded high magnification images (n =5–7 mice, adenomas=10–20), **p≤0.01, unpaired two-tailed t-test. Representative images to the right (100X, scale bars=25μm). (F) 100 days post-AOM, cleaved caspase 3-positive nuclei of *Apc*$^{Lrig1KO/+}$*Mpc1*^{Lrig1KO} and *Apc*$^{Lrig1KO/+}$ adenomas (black arrows) were quantified on blinded high magnification images (n =5–7 mice, adenomas=13–15, 100X, scale bars=25 μm), n.s.=not significant, unpaired two-tailed t-test. Green dashed circle indicates crypt necrosis and these positive nuclei were omitted. (G) At 49 days post-AOM, regions of superficial inflammation, epithelial injury with active inflammation (AI), aberrant foci, and low-grade dysplasia assessed by pathologic grading in colons of *Mpc1*$^{Lrig1KO/+}$, *Mpc1*$^{Lrig1KO/+}$, and control mice (n=8–10 mice), n.s.=not significant, unpaired t-test on number of microscopic lesions per mouse.

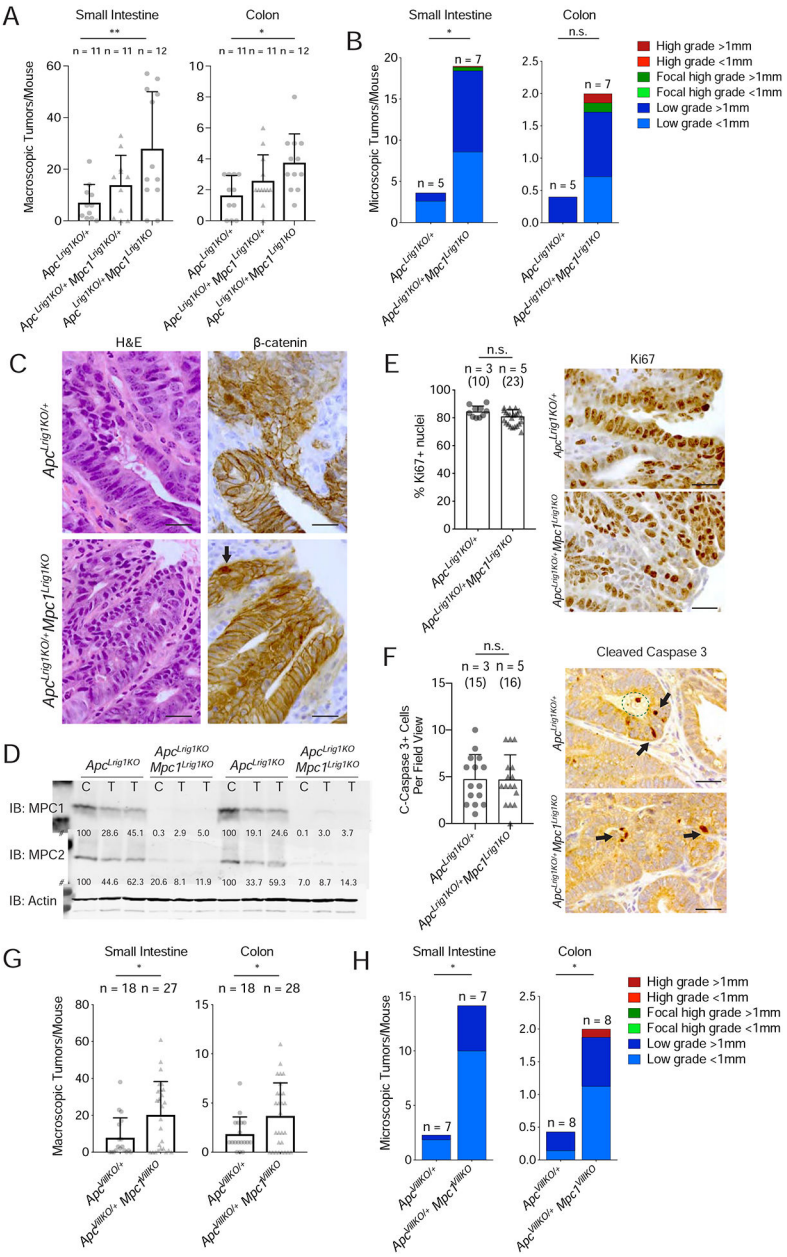

Figure 3: *Mpc1* deletion in the small intestine and colon increases dysplastic initiation in the *Apc* loss model of carcinogenesis.

(A) Macroscopic tumor burden was assessed in *Apc* $^{Lrig1KO/+}$*Mpc1*^{Lrig1KO}, *Apc* $^{Lrig1KO/+}$*Mpc1*$^{Lrig1KO/+}$, and *Apc* $^{Lrig1KO/+}$ mice at 90 days post-TAM (n=11–12 mice), **p≤0.01, *p≤0.05, one-way ANOVA with multiple comparisons (B) Microscopic tumor grade and size assessed by pathologic grading in the small intestine (left) and the colon (right) for *Apc*$^{Lrig1KO/+}$ *Mpc1*^{Lrig1KO} and *Apc*$^{Lrig1KO/+}$ mice (n=5–7), n.s.=not significant, *p≤0.05, unpaired t-test on number of microscopic tumors per mouse. (C) Hematoxylin/Eosin, and anti-β-catenin staining of *Apc*$^{Lrig1KO/+}$ and *Apc*$^{Lrig1KO/+}$ *Mpc1*^{Lrig1KO} adenomas (100X, scale bars=25 μm). Black arrows indicate nuclear β-catenin. (D) Immunoblot of paired normal crypts (“C”) and tumor (“T”) samples from two *Apc*$^{Lrig1KO/+}$ mice and two

$Apc^{Lrig1KO/+}Mpc1^{Lrig1KO}$ mice for MPC1, MPC2, and actin. Densitometry for MPC1 and MPC2, normalized to actin is shown with relative values adjusted to 100 for each $Apc^{Lrig1KO/+}$ mouse normal crypt sample. (E) 90 days post-tamoxifen, Ki67-positive nuclei as a percentage of total adenoma nuclei of $Apc^{Lrig1KO/+}Mpc1^{Lrig1KO}$ and $Apc^{Lrig1KO/+}$ adenomas were quantified on blinded high magnification images (n =3–5 mice, adenomas=10–23), n.s.=not significant, unpaired two-tailed t-test. Representative images to the right (100X, scale bars=25 μm). (F) 90 days post-tamoxifen, cleaved caspase 3-positive nuclei of $Apc^{Lrig1KO/+}Mpc1^{Lrig1KO}$ and $Apc^{Lrig1KO/+}$ adenomas (black arrows) were quantified on blinded high magnification images (n =3–5 mice, adenomas = 15–16), n.s.= not significant, unpaired two-tailed t-test. Representative images to the right (100X, scale bars = 25 μm). Green dashed circle indicates crypt necrosis and these positive nuclei were omitted. (G) At 140 days post-TAM, macroscopic tumor burden per mouse in $Apc^{VillKO/+}$ and $Apc^{VillKO/+}Mpc1^{VillKO}$ was assessed (n=18–27,28: one small intestine was damaged during dissection and removed from analysis). *p≤0.05, unpaired t-test. (H) Microscopic tumor grade and size assessed by pathologic grading in the small intestine (left) and colon (right) of $Apc^{VillKO/+}$ and $Apc^{VillKO/+}Mpc1^{VillKO}$ mice (n=7–8), *p≤0.05, unpaired t-test on number of microscopic tumors per mouse.

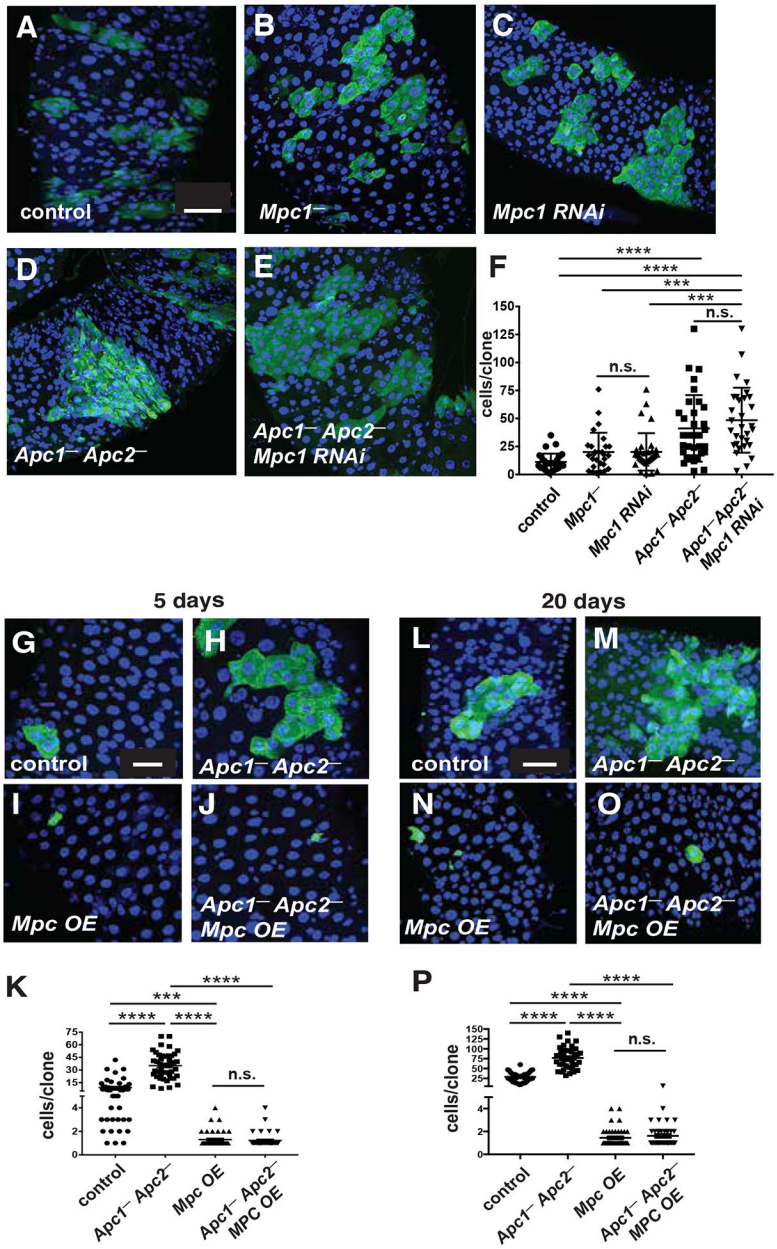

Figure 4. *MPC* overexpression arrests *Apc* mutant tissue hyperplasia.

Intestinal MARCM clones were generated using (A, G, L) an *FRT82B* wild-type chromosome (control), (B) a mutant chromosome for *dMpc1*, (C) a chromosome expressing *Tub>dMpc1* RNAi, (D, H, M) a chromosome mutant for *Apc1* and *Apc2*, (E) a chromosome mutant for *Apc1* and *Apc2* with *Tub>dMpc1* RNAi (I, N), a *Tub>dMpc1-dMpc2* overexpressing chromosome, and (J, O) an *Apc1* and *Apc2* mutant chromosome with *Tub>dMpc1-dMpc2* overexpression. Clones were analyzed either 5 days (A-K) or 20 days (L-P) after induction. Quantitation of GFP+ clone size for each genotype is shown (F, K, P). Clones are marked by GFP (green) and nuclei are stained with DAPI (blue). The reduced effect of *dMpc1* mutation alone or *dMpc1* RNAi on clone size in panel F is less than that reported earlier because these clones were examined at five days after clone induction rather

than 30 days (Schell et al., 2017). n≥30 intestines. ****p≤0.0001, ***p≤0.001, n.s.= not significant. Scale bars represent 50 μm (A), 20 μm (G), 40 μm (L).

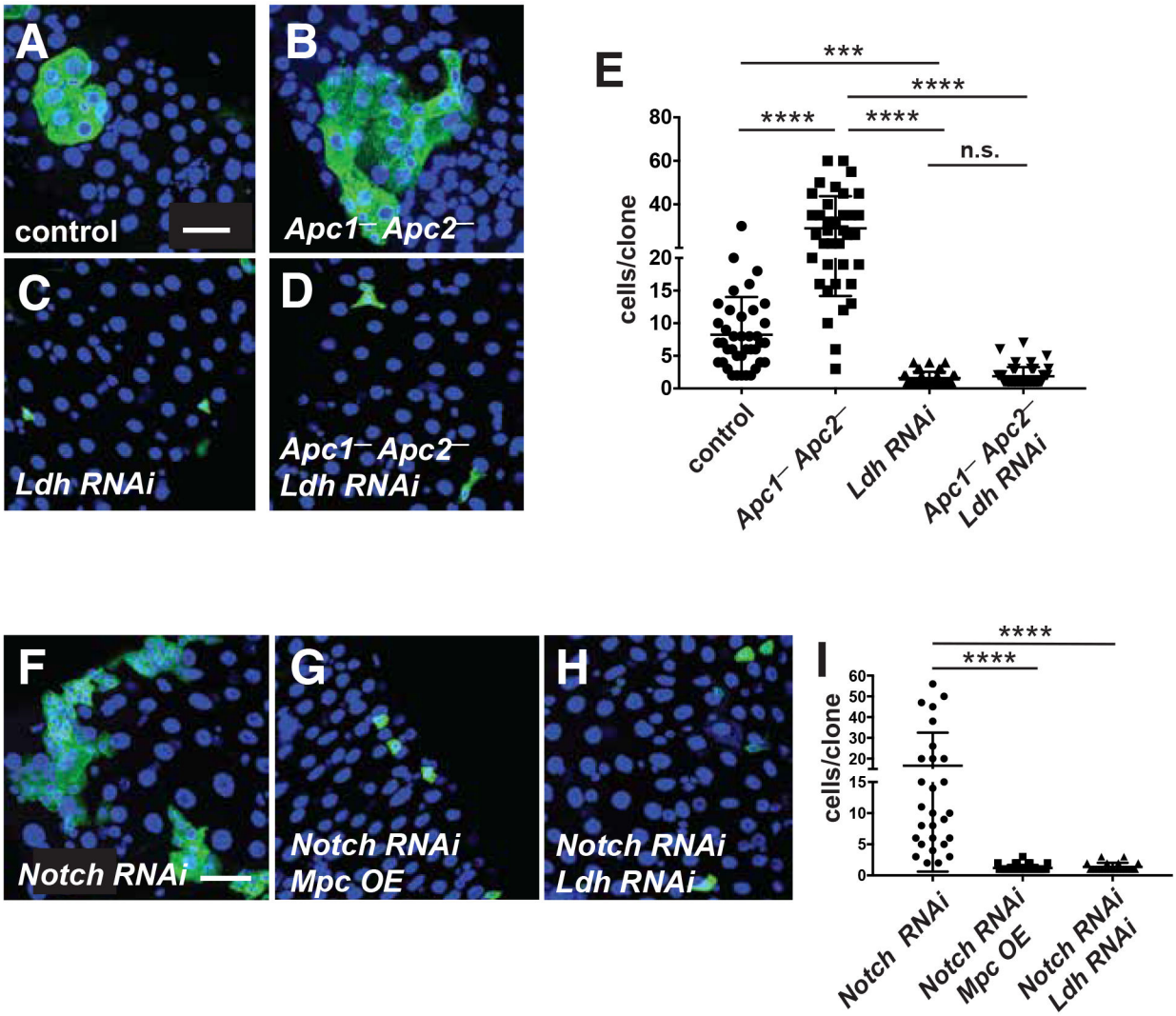

Figure 5. Increased mitochondrial pyruvate metabolism arrests *Apc* mutant tissue hyperplasia and blocks *Notch* enteroendocrine tumor expansion.

Intestinal MARCM clones were generated using (A) an *FRT82B* wild-type chromosome (control), (B) an *Apc1* and *Apc2* mutant chromosome, (C) a *Tub>LDH RNAi* chromosome (*LDH RNAi*), (D) an *Apc1* and *Apc2* mutant chromosome with *Tub>LDH RNAi*, and (F-H) a chromosome that expresses *Tub>Notch* RNAi either alone (F) or together with *Tub>dMpc1-dMpc2* overexpression (G) or *Tub>LDH RNAi* (H). Quantitation of GFP+ clone size for each genotype is shown (E, I). Clones are marked by GFP (green) and nuclei are stained with DAPI (blue). n≥30 intestines. ****p≤0.000, n.s.= not significant. Scale bars represent 30 μm (A, F).

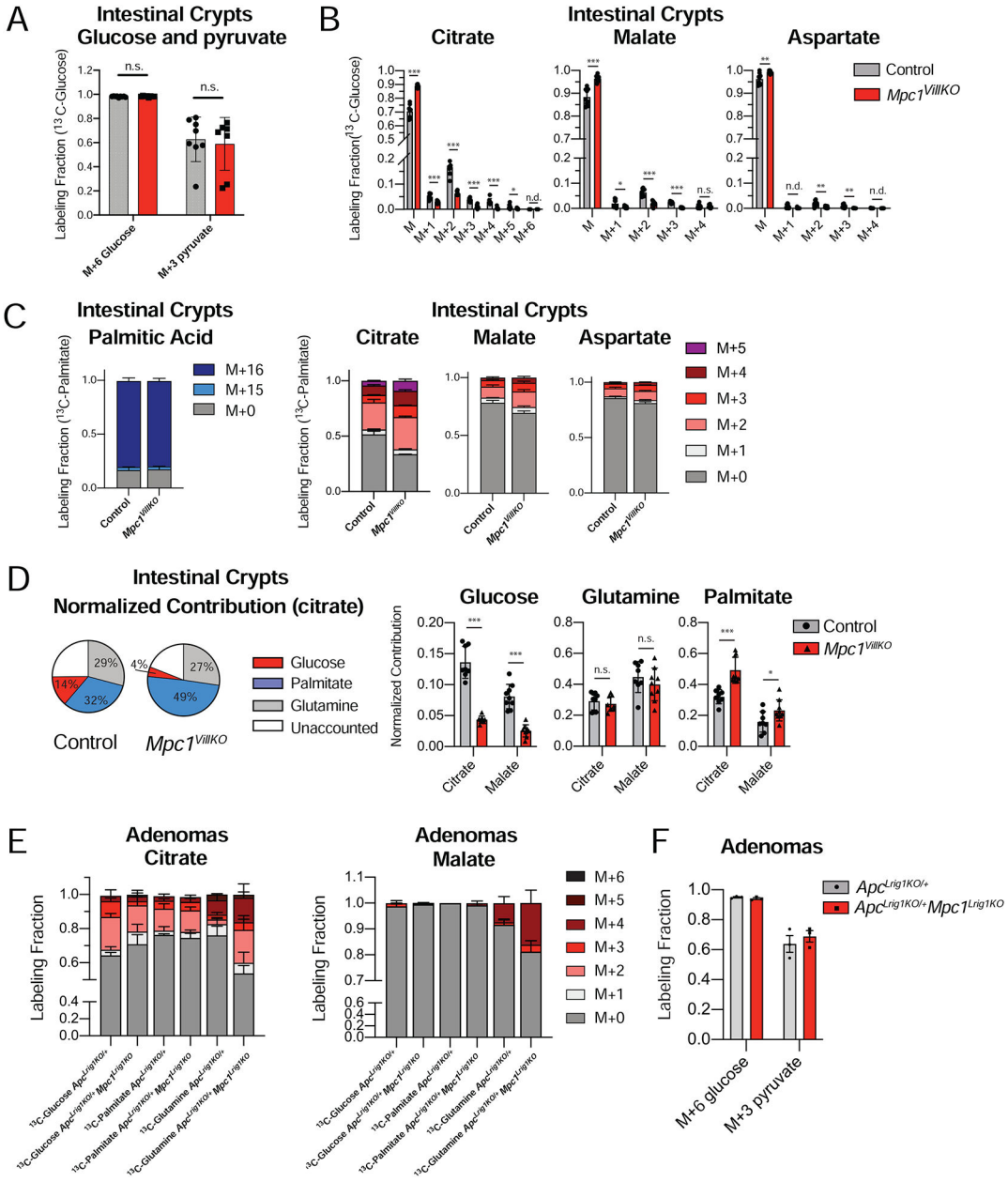

Figure 6. *Mpc1* loss influences fuel choice in intestinal crypts and adenomas.

Intestinal crypts or micro-dissected adenomas were freshly isolated and traced in parallel for each of three heavy labeled medias containing glucose, palmitate, and glutamine for 90 minutes. (A) Glucose (M+6) and pyruvate (M+3) labeling as measured by LC-MS from incubation with uniformly labeled ^{13}C-glucose is not different in crypts isolated from control and *Mpc1*^{VillKO} mice (n=8–9) n.s.= not significant, unpaired t-test (B) ^{13}C-Glucose labeling into TCA cycle products citrate, malate and aspartate is significantly reduced in *Mpc1*^{VillKO} crypts (n=8–9) ***p≤0.001, **p≤0.01, *p≤0.05, n.s. = not significant, n.d.= not determined, unpaired t-test. (C) ^{13}C-Palmitate M+16 labeling is not different between control and *Mpc1*^{VillKO} crypts (left). ^{13}CPalmitate labeling into TCA cycle products citrate, malate and aspartate is higher in *Mpc1*^{VillKO} crypts (n=8–9) (right). (D) Normalized

contribution of each nutrient (palmitate, glucose and glutamine) to citrate (highlighted in pie chart) and malate production in control and *Mpc1*^{VillKO} crypts. For each metabolite, a normalized labeling fraction was calculated and then corrected for the abundance of the isotopic precursor present in the isolated crypts (n=8,9) ***p≤0.001, *p≤0.05, n.s. = not significant, unpaired t-test. (E) Labeling of TCA intermediates citrate and malate as determined by GC-MS from heavy glucose, palmitate or glutamine containing media in freshly isolated adenomas from *Apc*$^{Lrig1KO/+}$ or *Apc*$^{Lrig1KO/+}$*Mpc1*^{Lrig1KO} mice 90 days post-TAM. The glutamine labeling fraction into citrate and malate increases in *Mpc1*^{Lrig1KO} mice (n=3). It is noteworthy that while the Cre driver is different between the normal crypts and adenomas, it is unlikely to affect the results as they are both efficient at causing complete recombination throughout the intestinal epithelium within a week of tamoxifen treatment. (F) Glucose (M+6) and pyruvate (M+3) labeling with uniformly labeled ^{13}C-glucose is not different in adenomas isolated from control and *Mpc1*^{Lrig1KO} mice (n=3 mice, pooled tumors >3 per mouse), n.s.= not significant, unpaired t-test.

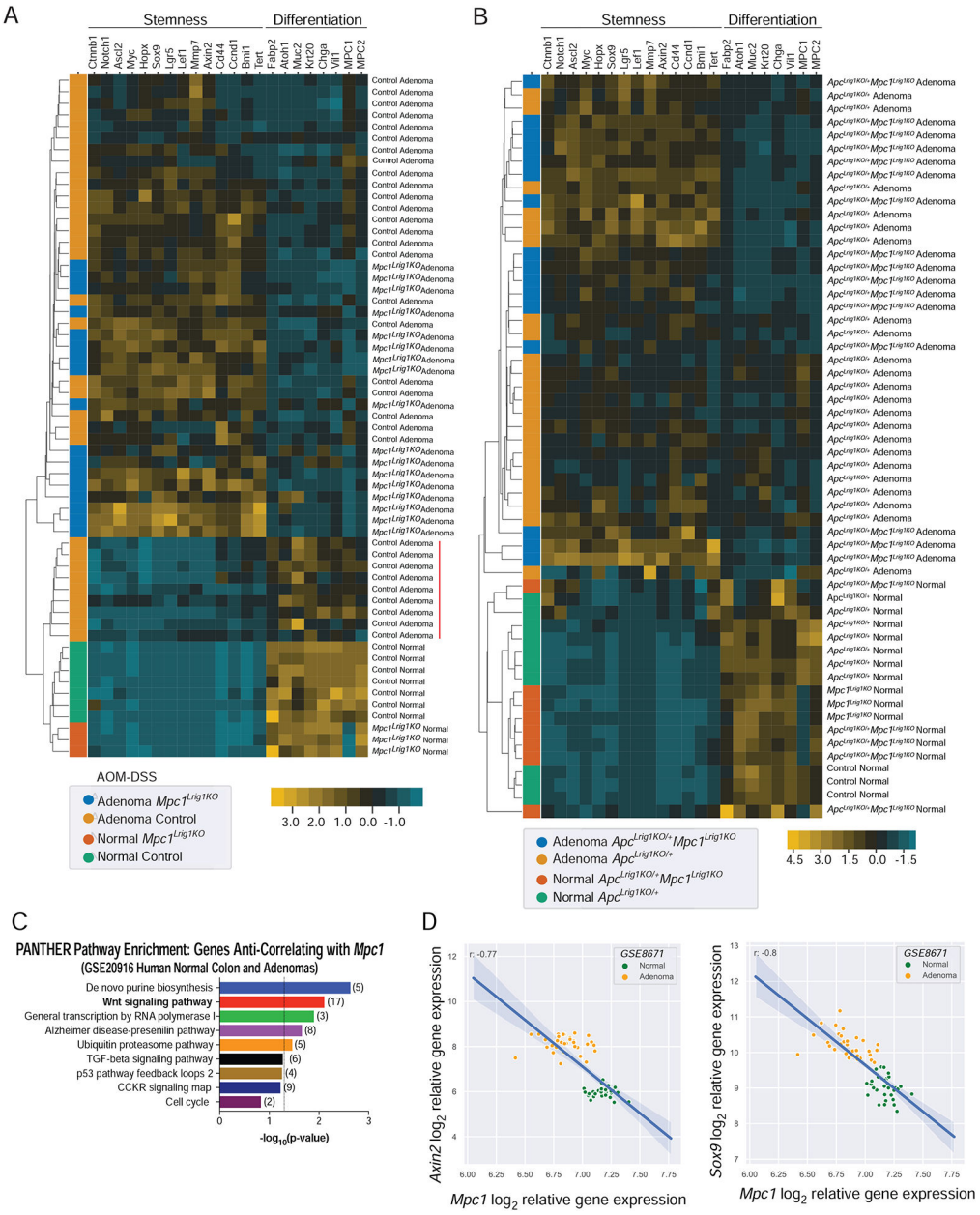

Figure 7. *Mpc1* deletion elicits enhanced stemness in adenomas and *Mpc1* anti-correlates with stemness in mouse and human adenomas.

(A-B) Adenoma tissue (orange and blue; n=16–32) and normal uninvolved colon epithelium (green and red; n=3–10) were isolated from AOM-DSS day 100 mice (A) and $Apc^{LrigKO/+}$ and $Apc^{LrigKO/+}Mpc1^{LrigKO/+}$ mice at 90 days post-TAM (B). RNA was extracted and evaluated on the 22-gene custom gene set including stemness and differentiation markers (top) and abundance displayed according to the heat map shown. Samples were clustered via calculating the Euclidean distance between centroids. See Berg 2019 for raw data and analysis code. (C) Linear least squares regression of *Mpc1* gene expression was performed using the adenoma and normal colon samples from GSE201916 and the resulting derived gene list showing *Mpc1* anti-correlation (r<−0.6; p-value < 0.01) was analyzed by

PANTHER (v13.1). Negative $\log_{10}$(p-values) are reported for each pathway with the number of pathway genes identified in parentheses. The dotted line marks the significance of pathway overrepresentation ($-\log_{10}(0.05) = 1.3$). See Berg 2019 for associated tables. (D) GSE20916-derived joint plots of relative gene expression for *Mpc1* versus Wnt pathway genes *Axin2* (left, p=1.25E-12) and *Sox9* (right, p=3.12E-10). The r-value and the fitted regression line with the slope's 95% confidence interval for each correlation are shown.

KEY RESOURCES TABLE

REAGENT or RESOURCE	SOURCE	IDENTIFIER
Antibodies		
Mouse monoclonal anti-Pros	Developmental Studies Hybridoma Bank #MR1A	RRID:AB_2722117
Rabbit *Drosophila* MPC1 and MPC2	Gift from William McDonald. Metabolic solutions development company. Kalamazoo, MI.	Colca et al., 2013
Chicken GFP	Abcam #13970	RRID:AB_300798
Alexa anti-chicken 488- conjugated secondary	Abcam #150169	RRID:AB_2636803
anti-mouse Cy3-conjugated secondary	Jackson Immunoresearch #715– 165151	RRID:AB_2315777
anti-rabbit Cy3-conjugated secondary	Jackson Immunoresearch #715– 165152	RRID:AB_2307443
MPC1 (IHC) 1:200	Sigma Aldrich HPA045119	RRID:AB_10960421
MPC1 (Immunoblots) 1:1000	Cell Signaling #14462	RRID:AB_2773729
MPC2 (Immunoblots) 1:1000	Cell Signaling #46141	RRID: AB_2799295
Ki67 (IHC) 1:600	Abcam, rabbit polyclonal, ab15580	RRID:AB_393778
b-catenin (IHC) 1:200	BD Biosciences #610153	RRID:AB_397554
Actin (immunoblots) 1:1000	Millipore MAB1501	RRID: AB_2223041
Cleaved Caspase 3 (IHC) 1:100	Cell Signaling #9664	RRID: AB_2070042
H2A.X (IHC) 1:500	Cell Signaling #2595	RRID: AB_10694556
Phospho-H2A.X (IHC) 1:500	Cell Signaling #5438	RRID: AB_10707494
Biotin-SP-AffiniPure Donkey Anti-Rabbit IgG (H+L) antibody 1:100	Jackson Immunoresearch #711-065-152	RRID:AB_2340593
Biotin-SP-AffiniPure Donkey Anti-Mouse IgG (H+L) 1:100	Jackson Immunoresearch #715–065150	RRID:AB_2307438
Biotin-SP-AffiniPure Donkey Anti-Rat IgG (H+L) 1:100	Jackson Immunoresearch #712-065-153	RRID:AB_2315779
Goat Anti-Mouse IgG (H&L) Antibody Dylight™ 800 Conjugated (immunoblots)	Rockland #610-145-002-0.5	RRID:AB_10703265
Donkey anti-Rabbit IgG (H+L) Highly Cross-Adsorbed Secondary Antibody, Alexa Fluor 680 (immunoblots)	Invitrogen #A10043	RRID:AB_2534018
Chemicals, Peptides, and Recombinant Proteins		
Tamoxifen	Sigma Aldrich T5648	N/A
Azoxymethane	Sigma Aldrich A5486	N/A
Dextran Sodium Sulfate	USB/Affymetrix 14489	N/A
Fluorescein-isocyannate-dextran	Sigma Aldrich 46945	N/A
VectaStain ABC Elite	VectorLabs PK6100	N/A
DAB substrate	VectorLabs SK4100	N/A
hematoxylin	Sigma Aldrich GHS316	N/A
Permount	Fisher Chemical SP15	N/A
5-bromo-2’-deoxyuridine	Invitrogen b23151	N/A
Vector Antigen Unmasking	VectorLabs H3300	N/A
Solution		
Donkey Serum	Jackson Immunoresearch #017-000-001	N/A

REAGENT or RESOURCE	SOURCE	IDENTIFIER
AffiniPure Fab donkey antimouse fragments	Jackson Immunoresearch #715-007-003	N/A
Mammalian Protease Inhibitor Cocktail	Sigma Aldrich P8340	N/A
PhosSTOP	Roche Molecular 04906845001	N/A
Peanut Oil	Sigma Aldrich P2144	N/A
Phosphate Buffered Saline	Invitrogen 10010049	N/A
U-^{13}C-L-Glutamine	Cambridge, CLM-1822	N/A
U-^{13}C-Glucose	Cambridge, CLM-1396	N/A
U-^{13}C -Palmitate	Cambridge, CLM-409	N/A
L-Glutamine	Sigma Aldrich G3126	N/A
D-Glucose	Sigma Aldrich G8270	N/A
Sodium Palmitate	Sigma Aldrich P9767	N/A
Bovine Serum Albumin (Ultra Fatty Acid Free)	Roche, CN 03 117405 001	N/A
DMEM (base powder), supplemented with Amino Acids	US Biological D9800–27	N/A
Murine EGF	Peprotech #315–09	N/A
Murine Noggin	Peprotech #250–38	N/A
Murine Wnt-3a	Peprotech #315–20	N/A
CHIR99021	Tocris #4423	N/A
N-acetyl cysteine	Sigma Aldrich A7250	N/A
L-carnitine	Sigma Aldrich C0283	N/A
Matrigel	Fisher Scientific #356321	N/A
Vectashield mounting medium	Vector, Laboratories. USA H1200	N/A
Formaldehyde 16% Ultra pure EM grade	Polysciences Inc, #18814–10	N/A
Critical Commercial Assays		
Qiagen FFPE Rneasy kit	Qiagen cat: 73504	RRID:SCR_008539
nCounter Elements 60-Plex TagSet (ELE-060-P1TS)	Nanostring Technologies// Schell et al. 2017 *Nat Cell Bio*	N/A
Deposited Data		
Nanostring Mouse Colon crypt and adenoma RNA data	GSE136710	N/A
Experimental Models: Cell Lines and Drosophila lines		
UAS-dMpc1 RNAi	Vienna Drosophila resource center	VDRC: 102734
UAS-LDH RNAi	Vienna Drosophila resource center	VDRC: 102330
UAS-Notch RNAi	Bloomington Drosophila Stock Center	BDSC:7078
UAS-dMpc1-P2A-dMpc2	Generated in the Thummel Lab, (Schell et al 2017)	N/A
w[*]; P{ry[+t7.2]=neow[*]; P{ry[+t7.2]=neoFRT}82B sr[1] e[1] Apc2[N175K] Apc[Q8]/TM3, P{w[+mC]=ActGFP}JMR2, Ser[1]FRT}82B sr[1] e[1] Apc2[N175K] Apc[Q8]/TM3, P{w[+mC]=ActGFP}JMR2, Ser[1]	Bloomington Stock center	BDSC: 7211

REAGENT or RESOURCE	SOURCE	IDENTIFIER
hs-flp, UAS-GFP, + ; *Tub-GAL4, FRT82B, TubGal80/TM6C*	Washington University in St. Louis, Gift from Craig Micchelli	N/A
Mpc1$^{flox/flox}$ mice (C57bl6)	Rutter Lab	N/A
Villin^{CreER} mice (C57bl6)	Yilmaz Lab	N/A
Lrig1^{CreER} mice (C57bl6)	Jackson Laboratory Stock No: 018418	RRID:IMSR_JAX:018418
Apc$^{loxp\ exon\ 14}$ (C57bl6)	Yilmaz Lab	N/A
Software and Algorithms		
XPRESStools v.0.0.2b1	DOI: 10.5281/zenodo.2581696	N/A
Python Software Foundation. Python Language Reference, version 3.6.	Available at http://www.pvthon.org	RRID:SCR_008394
Eric Jones and Travis Oliphant and Pearu Peterson and others, SciPy: Open source scientific tools for Python, 2001	http://www.scipy.org/	RRID:SCR_008058
AltAnalyze	http://www.altanalyze.orq/	RRID:SCR_002951
GEOparse v1.1.0Other	https://github.com/guma44/GEOparse	N/A